Ocean Engineering 329 (2025) 121116

Contents lists available at ScienceDirect

Ocean Engineering

journal homepage: www.elsevier.com/locate/oceaneng

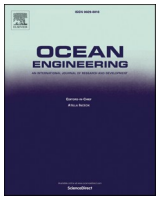

Research paper

Improving power stability in floating offshore wind turbines through control systems: An aero-hydro-servo-elastic study

Yang Huang [a], Qing Xiao [a,*], Decheng Wan [b]

[a] Department of Naval Architecture, Ocean & Marine Engineering, University of Strathclyde, Glasgow, UK
[b] Computational Marine Hydrodynamics Lab (CMHL), School of Naval Architecture, Ocean and Civil Engineering, Shanghai Jiao Tong University, Shanghai, China

ARTICLE INFO

Keywords:
Floating offshore wind turbine
Generator torque controller
Blade pitch controller
Coupled aero-hydro-servo-elastic responses
Computational fluid dynamics

ABSTRACT

Floating offshore wind turbines (FOWTs) exhibit significant potential for renewable energy generation. However, due to the six-degree-of-freedom (6DoF) motions of their platforms, they experience greater inflow wind speed variations than bottom-fixed turbines. This variability poses challenges to power output stability, underscoring the critical role of advanced control systems. Building upon our previous extensive studies on FOWT dynamics, this research investigates the coupled dynamic responses of FOWTs equipped with generator torque and blade pitch controllers. A fully coupled aero-hydro-servo-elastic analysis framework, integrated with Computational Fluid Dynamics (CFD), is employed to simulate a spar-type FOWT under diverse wind speeds and sea states. The study analyses key parameters including aerodynamic loads, aeroelastic blade deformation, platform motions, mooring tensions, and wake field characteristics, focusing on the controllers' impact on energy performance and structural dynamics. Results demonstrate that the controllers effectively mitigate aerodynamic load fluctuations and enhance power output when wind speeds exceed the rated value. While the controllers increase platform motion at high wind speeds, they significantly suppress motion responses under severe wave conditions. An inverse relationship is observed between wake velocity modifications and average aerodynamic power variations due to controller interventions. Notably, except at a high wind speed of 18 m/s, the controllers amplify turbulence intensity within the wake, particularly in the proximal wake region ($x/D < 3$). These insights contribute to optimizing control strategies for FOWTs, enhancing their efficiency and reliability in renewable energy generation under varying operational conditions.

1. Introduction

Driven by the pursuit of renewable energy, the wind power industry is expanding from onshore to offshore to harness the vast potential of marine environments. Offshore wind power, characterized by higher and more stable wind speeds, is advancing from nearshore to deep-sea installations (Díaz and Soares, 2020). This evolution necessitates the transition from land-based wind turbines to offshore fixed and floating counterparts. Floating offshore wind turbines (FOWTs) represent the frontier of this shift, addressing the challenges of deploying wind power in deep-water environments where traditional fixed foundations are impractical (Bošnjaković et al., 2022).

Compared to fixed wind turbines, FOWTs are mounted on platforms that allow six degrees of freedom (6DoF) in motion. These movements can cause significant fluctuations in inflow wind speeds, reducing power generation efficiency and output stability (Tran and Kim, 2015a, 2015b). To mitigate these issues, control strategies such as generator torque (GT) controllers and blade pitch (BP) controllers are more crucial for FOWTs than for onshore turbines (López-Queija et al., 2022). Therefore, investigating the coupled responses of FOWTs with these control systems is crucial for enhancing the efficiency and reliability of FOWTs, thereby contributing to the broader adoption of offshore wind energy as a sustainable energy source.

Accurately predicting the coupled dynamic responses of FOWTs is challenging due to the system's complexity, involving interactions among the wind turbine, floating platform, mooring system, control system, and other components. Researchers have developed several numerical models with varying levels of accuracy (Otter et al., 2022). In the initial design phases of FOWTs, where precision requirements are relatively low, linear models (Hegseth and Bachynski, 2019; Karimi et al., 2017; Pegalajar-Jurado et al., 2018) are typically used to quickly provide a general overview of rigid-body motion dynamics. These

* Corresponding author.
E-mail address: qing.xiao@strath.ac.uk (Q. Xiao).

https://doi.org/10.1016/j.oceaneng.2025.121116
Received 10 December 2024; Received in revised form 16 March 2025; Accepted 29 March 2025

models are useful for assessing global stability but cannot capture structural deformation responses. To evaluate the global dynamics of FOWT designs at more advanced stages, higher-accuracy models based on the potential flow method are employed. Aerodynamic calculations utilize the blade element momentum theory (BEMT) (Manwell et al., 2010), generalized dynamic wake (GDW) method (Suzuki and Hansen, 1999), and free vortex wake (FVM) method (Sebastian and Lackner, 2012). Hydrodynamic predictions use the potential flow method, the Morison equation (Sarpkaya, 1981), or a combination of both. For structural analysis, dynamic and quasi-static approaches are applied to mooring lines, while finite element method (FEM) and modal analyses assess structural dynamics. These models meet the precision requirements of engineering applications while maintaining relatively high computational efficiency, making them widely used in engineering tools such as OpenFAST (NREL), HAWC2 (DTU), Bladed (DNV), Orcaflex (Orcina), Flexcom (Wood Group), and SIMA (MARINTEK. SIMA, 2016). The Offshore Code Comparison Collaboration project series (Cordle and Jonkman, 2011; Robertson et al., 2014, 2017, 2020) has conducted comparative studies among these tools, exploring different FOWT designs, including spar and semi-submersible types.

To better predict the complex dynamic responses of FOWTs, high-accuracy models employing Computational Fluid Dynamics (CFD) for fluid dynamics and the FEM for structural dynamics are increasingly favoured. These models are particularly valued for their precision in analysing local flow phenomena and nonlinear structural deformations, especially under extreme conditions. They effectively capture dynamic inflow effects, nonlinear responses, and complex wake characteristics (López-Queija et al., 2022). Liu et al. (2017) developed a sophisticated fluid-structure interaction (FSI) analysis tool using OpenFOAM (Jasak, 2009) and a multibody dynamics (MBD) code (MBDyn, 2024, 2024) for FOWTs with aero-elastic blades. This tool was used to investigate the OC4 DeepCWind semi-submersible FOWT model under various operating conditions. Tran and Kim, 2016, 2018, Zhang and Kim (2018) conducted detailed analyses on the same model using STAR-CCM+ (Sabalcore. StarCCM, 2024), uncovering complex fluid phenomena such as blade-tip vortices, vortex shedding, interference effects between the tower and blades, and turbulent wakes. However, CFD methods employing blade-resolved models requires significant computational resources, as demonstrated by Tran and Kim, 2016, 2018, and Zhang and Kim (2018). To address this, Cheng et al. (2019) introduced an unsteady actuator line model (ALM) (Troldborg, 2009; Li et al., 2015) as a computationally efficient alternative for aerodynamic calculations. By replacing physical wind turbine blades with virtual actuator lines represented by a source term, the aerodynamic study is streamlined, resulting in considerable time savings. This innovative model has also been used to explore wake interactions between two FOWTs (Huang et al., 2022, 2023).

Given the complex dynamic inflow conditions faced by FOWTs, CFD methods offer greater accuracy in simulating the coupled response of FOWTs equipped with control systems. However, implementing control systems in CFD methods is challenging. Common control strategies dynamically adjust the rotor speed and blade pitch angle based on inflow wind speed to enhance power generation efficiency and minimize power variations. In blade resolved CFD methods, real-time adjustments of rotor speed and pitch angle require complex dynamic mesh handling, posing significant demands on computational stability and resources. In contrast, potential flow-based models can more easily integrate control systems through real-time parameter adjustments. Consequently, most research on FOWTs with control systems is conducted using potential flow-based models. A series of studies based on OpenFAST have investigated the aerodynamic loads and platform motion of various FOWT types using different control strategies, including blade-pitch and mass-spring-damper mechanisms (Shah et al., 2021; Ha et al., 2021; Truong et al., 2022).

There are a few studies that integrate FOWT control systems into the CFD approach. Quallen and Xin (Quallen and Xing, 2016) developed a fully coupled FOWT simulation tool that combines a variable-speed GT controller with the CFD solver CFDShip-Iowa (Paterson et al., 2003). However, their model did not incorporate a blade pitch (BP) controller and only considered a single uniform wind speed and regular wave conditions. To simplify the implementation of control systems in CFD approaches, body force methods such as the ALM are used for aerodynamic calculations. Since ALM calculates aerodynamic loads based on BEMT, control systems can be conveniently incorporated by dynamically adjusting the rotor speed and blade pitch angle. Yang et al. (2023) examined the wake characteristics of a variable-speed pitch-regulated FOWT using a CFD method that integrates the actuator curve embedding method with collective blade pitch control strategies. Their study accounted for prescribed surge motions but excluded the six-degrees-of-freedom (6DoF) motions of the floating platform.

In this study, an aero-hydro-servo-elastic analysis tool (Huang, 2021) is employed to investigate the dynamic responses of a spar-type FOWT with 6DoF motions, incorporating GT and BP controllers. CFD and FEM approaches are used to predict fluid and structural dynamics, respectively. A modified ALM is selected to enhance aerodynamic computational efficiency and facilitate the implementation of wind turbine control systems. Various wind speeds and sea states are considered. By analysing aerodynamic loads, flexible blade deformation, platform motions, mooring tensions, and wake field characteristics, the influence of the controllers on the FOWT's performance is examined across a range of wind speeds and sea states. The insights gained from this study aim to enhancing the FOWT's efficiency and reliability under varying operational conditions.

While this study primarily focuses on the influence of the wind turbine control system, including the GT and BP controllers, it is worth noting that floating platform control systems also play a crucial role in regulating platform motions. Active control strategies, such as station-keeping systems and motion damping control, are employed to reduce excessive platform motions and enhance turbine performance stability. Although platform control is beyond the scope of this study, its impact on FOWT dynamics remains an essential aspect for future research.

This paper is structured as follows: Section 2 outlines the coupled analysis tool used for the simulations. Section 3 details the computational setup for simulating the FOWT. Section 4 analyses the computational results, emphasizing the coupled dynamic responses of the FOWT with control system across different wind and wave scenarios. Section 5 summarizes the impact of the control system on the performance of the FOWT based on the numerical results.

2. Coupled aero-hydro-servo-elastic analysis tool

In our previous work, we developed a coupled aero-hydro-elastic analysis tool for FOWTs using OpenFOAM (Huang, 2021). A modified ALM was used to predict the aerodynamic performance of wind turbines (Huang et al., 2021). Euler-Bernoulli beam theory, combined with the FEA method, was adopted to calculate blade deformation (Huang and Wan, 2020). The dynamic responses of the floating platform with mooring lines were computed using a CFD code (Liu et al., 2017; Wang et al., 2019). Wind turbine control strategies (Jonkman et al., 2009), including GT and BP controllers, were also implemented. Additionally, a two-way explicit coupling strategy was employed to achieve effective interaction between the wind turbine and the floating platform, as well as between the fluid and structure. Several studies have been conducted to validate the reliability of this tool (Huang, 2021; Huang et al., 2021; Cao and Wan, 2017; Zhuang and Wan, 2019; Wang and Wan, 2019). Compared to OpenFAST, which is widely used in engineering for FOWT simulations, the present tool employs CFD and FEM to predict the dynamic responses of FOWTs. As a result, it provides more detailed flow information and can handle more complex wind-wave conditions, albeit at the cost of significantly higher computational resources. Furthermore, the current tool is more easily extended to simulate wake interactions among multiple FOWTs.

In this study, we employ the above tool to investigate the coupled dynamic responses of a FOWT. Given the focus on wind turbine control strategies, this section introduces the analysis model along with the GT and BP controllers. Other comprehensive details on the aerodynamic, structural, and hydrodynamic models integrated into this tool are provided in Appendices A to C.

2.1. Coupled analysis model

2.1.1. Governing equations

To better capture the development of the turbine's wake, Large Eddy Simulations (LES) are performed in this study. The governing equations for LES are the spatially implicitly filtered Navier-Stokes equations.

$$\frac{\partial \overline{u}_i}{\partial t} = 0 \tag{1}$$

$$\frac{\partial \overline{u}_i}{\partial t} + \frac{\partial \overline{u}_i}{\partial x_j}\left(\overline{u}_i \overline{u}_j\right) = -\frac{1}{\rho}\frac{\partial \overline{p}_i}{\partial x_i} + \nu \frac{\partial^2 \overline{u}_i}{\partial x_i \partial x_j} - \frac{\partial \tau_{ij}}{\partial x_j} + \frac{1}{\rho}\left(f_\sigma + f_s + f_\varepsilon\right) \tag{2}$$

where $\overline{u}_i$ and $\overline{p}_i$ denote the resolved filtered velocity and pressure, respectively. ρ represents the mixture density of two fluids. The source terms f_σ, f_s, and f_ε correspond to surface tension, sponger layer damping, and wind turbine aerodynamic forces, respectively. The subgrid-scale (SGS) stress tensor, $\tau_{ij} = \overline{u_i u_j} - \overline{u}_i \overline{u}_j$, is modelled using the standard Smagorinsky model (Smagorinsky, 1963).

$$\tau_{ij} = -2\upsilon_{SGS}\overline{S}_{ij} \tag{3}$$

$$\upsilon_{SGS} = \left(C_s \Delta\right)^2 \left(2\overline{S}_{ij}\overline{S}_{ij}\right)^{1/2}, \overline{S}_{ij} = \frac{1}{2}\left(\frac{\partial \overline{u}_i}{\partial x_j} + \frac{\partial \overline{u}_j}{\partial x_i}\right) \tag{4}$$

where υ_{SGS} denotes the subgrid viscosity. The spatial filter $\Delta = (\Delta x \Delta y \Delta z)^{1/3}$ is defined by the grid sizes Δx, Δy, and Δz in the respective directions. The Smargorinsky coefficient C_s is set to 0.14, a value adopted from previous LES studies on wind turbine aerodynamics (Ning and Wan, 2019).

The fluid solver discretizes the governing equations in the fluid domain using the finite volume method. The Volume of Fluid (VOF) method is employed to capture the free surface. The PIMPLE algorithm, which combines Pressure Implicit with Splitting of Operator (PISO) and Semi-Implicit Method for Pressure-Linked Equations (SIMPLE), is utilized for pressure-velocity coupling. Temporal discretization is performed using a second-order Crank-Nicolson scheme, while convective terms are discretized using a second-order upwind scheme. Gradient terms are handled using a second-order cell-limited Gauss linear scheme.

2.1.2. Coupling schemes

Two aspects of coupling are considered in the simulation: the interaction among the wind turbine, floating platform, and mooring system, and the fluid-structure interaction between the wind turbine's aerodynamic response and blade deformation. Fig. 1 illustrates that bidirectional coupling is achieved through the transfer of displacement, velocity, and force. This includes accounting for blade position and changes in inflow wind speed due to platform motion in aerodynamic load calculations. The 6DoF motion response of the floating platform considers both wind turbine aerodynamic loads and mooring tensions. The platform's displacement also provides position data for mooring system analysis. Coupling between the wind turbine's aerodynamic response and blade deformation involves transfers of velocity, displacement, and load. Aerodynamic load calculations consider blade position and wind speed changes due to deformation, and these loads are incorporated as external forces in structural deformation calculations. All the coupling mechanisms use explicit schemes. Furthermore, the solving procedure for coupled aero-hydro-servo-elastic simulation of the FOWT is depicted in Fig. 2.

It is noted that both GT and BP controllers are integrated into the aerodynamic model to enable real-time adjustments of turbine rotational speed and blade pitch angle. A detailed illustration is provided in Appendix A.

2.2. Wind turbine control system

In this coupled analysis tool, the wind turbine control system (CS) includes GT and BP controllers. The GT controller remains active at all times, aiming to maximize power output by controlling generator torque as a function of rotor speed. The BP controller activates when the inflow wind speed is between the rated and cut-out speeds, serving to regulate power and reduce loads (Otter et al., 2022).

2.2.1. Generator torque controller

The procedure of GT controller is illustrated in Fig. 3. It is assumed that the wind turbine operates under inflow conditions with wind speeds lower than the rated speed. The inflow wind speed is denoted by u_{in}, the wind turbine rotor's rotational speed by Ω_{R}, the aerodynamic torque of the rotor by M_{R}, the generator's rotational speed and torque by Ω_{G}, and M_{G}, respectively. At this point, the rotor and the generator are in a stable equilibrium. The rotor and generator are connected through a gearbox, and the relationship between their rotational speeds and torques is as follows:

$$\Omega_{\text{G}} = \Omega_{\text{R}} \bullet R_{\text{GB}} \tag{5}$$

$$M_{\text{G}} = M_{\text{R}} \bullet E_{\text{GB}} / R_{\text{GB}} \tag{6}$$

where R_{GB} is the gear ratio between the generator and the turbine rotor, E_{GB} is the transmission efficiency from the rotor to the generator. When u_{in} changes to u'_{in}, M_{R} changes to M'_{R}. As a result, the balance between M'_{R} and M_{G} is disrupted, necessitating an adjustment in Ω_{R} to re-achieve a new equilibrium status. The rate of change in Ω_{R}, denoted as $\Delta\dot{\Omega}$, can be calculated using the following equation:

$$\Delta\dot{\Omega} = \left(M'_{\text{R}} \bullet E_{\text{GB}} - M_{\text{G}} \bullet R_{\text{GB}}\right) / I_{\text{D}} \tag{7}$$

where I_{D} represents the moment of inertia of the drive system.

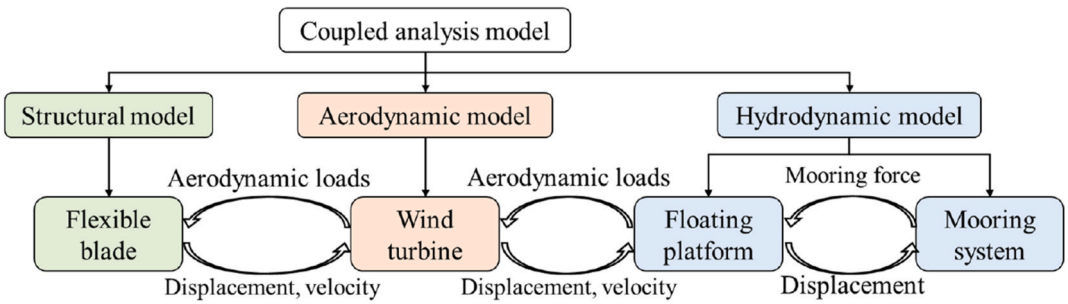

Fig. 1. Coupling variables in FOWT system.

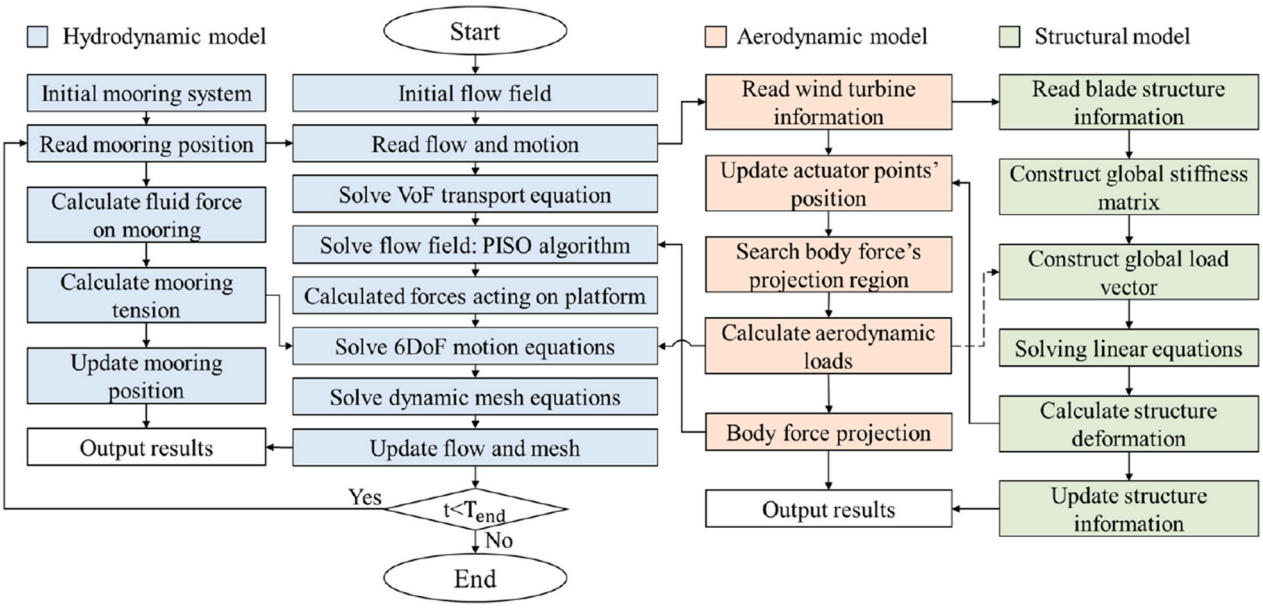

Fig. 2. Solving procedure of coupled aero-hydro-servo-elastic modelling of FOWT.

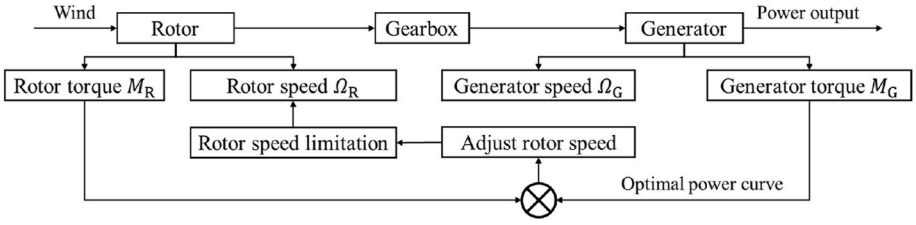

Fig. 3. Procedure of GT controller.

2.2.2. *Blade pitch controller*

Fig. 4 displays the main process of BP controller. It is assumed that the wind turbine operates steadily at rated wind speed, where Ω_R reaches the rated value (Ω_0), and M_R is in balance with M_G. As u_{in} increases, M_R will exceed M_G. To maintain the balance between M_R and M_G, the GT controller increases Ω_R, causing Ω_R to exceed Ω_0, thereby triggering the BP controller. The classic Proportional-Integral (PI) algorithm is employed to control the wind turbine blades' pitch angles (Jonkman et al., 2009). Notably, the derivative gain is omitted from the controller to prevent sudden dramatic changes in pitch angle due to wind speed fluctuations.

The change in blade pitch angle ($\Delta\theta$) can be calculated as follows:

$$\Delta\theta = K_P R_{GB}\Delta\Omega + K_I \int_0^t R_{GB}\Delta\Omega \mathrm{d}t \tag{8}$$

where $\Delta\Omega$ represents the difference between the actual and rated rotational speeds of the generator, serving as the input signal. K_P and K_I denote the proportional and integral increments of the input signal, respectively.

$$K_P = \frac{2I_D\Omega_0\xi_\varphi\omega_{\varphi n}}{R_{GB}\left(-\frac{\partial P}{\partial\theta}(\theta=0)\right)} GK(\theta) \tag{9}$$

$$K_I = \frac{I_D\Omega_0{\omega_{\varphi n}}^2}{R_{GB}\left(-\frac{\partial P}{\partial\theta}(\theta=0)\right)} GK(\theta) \tag{10}$$

where ξ_φ represents the damping coefficient, $\omega_{\varphi n}$ indicates the second-order natural frequency of the rotor, $\partial P/\partial\theta(\theta=0)$ refers to the rate of change in output power at a 0° pitch angle under rated speed conditions, and $GK(\theta)$ represents a correction factor. A collective pitch control strategy is adopted, meaning all blades have the same pitch angle. More details about the BP controller can be found in the literature (Jonkman et al., 2009).

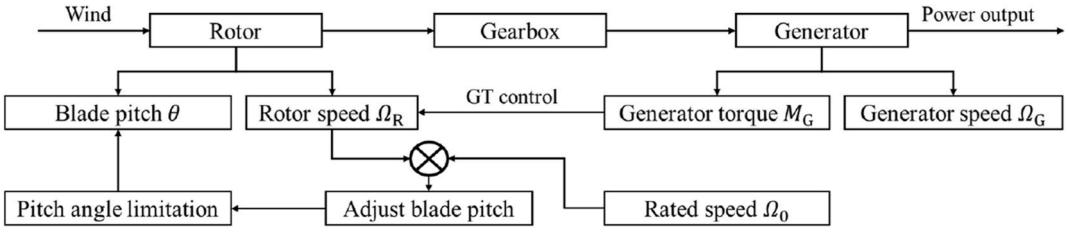

Fig. 4. Procedure of BP controller.

3. Numerical simulation set up

3.1. FOWT model

A spar-type FOWT model from the OC3 project is investigated in this study. It consists of the NREL 5-MW turbine, the OC3-Hywind Spar platform, and a catenary mooring system. The NREL 5-MW turbine, designed by the NREL for large offshore wind turbines, features a rotor diameter of 126 m, a hub height of 90 m, a rated rotational speed of 12.1 rpm, and cut-in, cut-out, and rated wind speeds of 3 m/s, 25 m/s, and 11.4 m/s, respectively. The OC3-Hywind Spar platform, equipped with a catenary mooring system, is designed for deep-sea FOWTs. The schematic diagram of the FOWT and its main geometric parameters are shown in Fig. 5. More detailed information can be found in the literature (Jonkman et al., 2009; Jonkman, 2010).

This wind turbine employs GT and BP controllers and uses a "five-region" torque control method to ensure continuous and stable rotational speed (Jonkman et al., 2009). This method modulates the turbine's rotational speed to match the generator's mechanical torque under varying wind conditions, as depicted in Fig. 6. The black line represents the theoretical torque-speed curve for maximum power output, while the blue line shows the torque-speed curve as implemented in actual control scenarios.

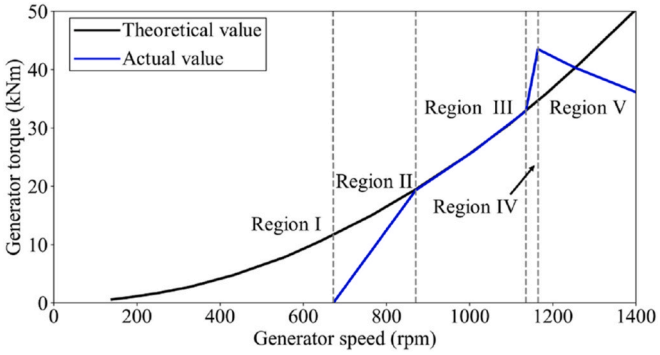

Fig. 6. Generator torque versus rotational speed in "five-region" control method.

3.2. Computational domain

As shown in Fig. 7, a cubic region with dimensions of 784 m (x) × 384 m (y) × 504 m (z) is generated in this numerical simulation. The water depth is set to 0.7 d (d = 320 m, the actual depth of water), at which the impact on platform motion can be ignored. The height of the air phase is set to 2.2D (D = 126 m, the rotor diameter) to account for turbine wake expansion. The FOWT is positioned at the centre of the computational domain, about 1.1 λ_w (λ_w = 147 m is the wavelength) from the inlet boundary and about 5D from the outlet boundary. The distance between the hub centre and the free surface is H_0 = 90 m. Additionally, a sponge layer with a length of 1.5 λ_w is established before the outlet boundary to absorb wave reflections.

Different mesh resolutions are employed within the computational domain, as depicted in Fig. 8. The mesh size in the x and y directions is set to 8 m. Near the free surface in the z direction, the mesh size is reduced to 2 m, while it gradually increases both upwards and downwards along the z-axis. To better capture the free surface and wake development and accurately calculate the platform's motion response, finer mesh resolutions are used near the free surface, within the wind turbine wake region, and around the platform. The minimum mesh size near the free surface is 2 m × 2 m × 0.5 m, and within the wake region near the blades, it is 2 m × 2 m × 2 m. This "large" mesh size near the wind turbine is used because virtual actuator lines simulate the wind turbine instead of a blade-resolved approach. The total number of

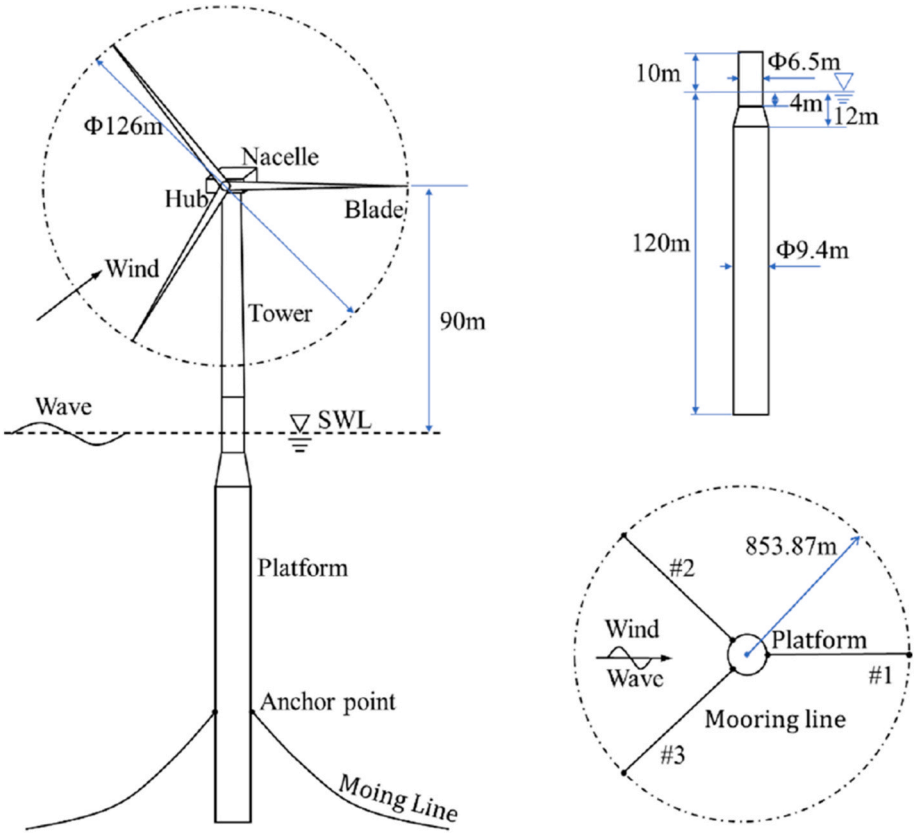

Fig. 5. Schematic diagram of the spar-type FOWT system.

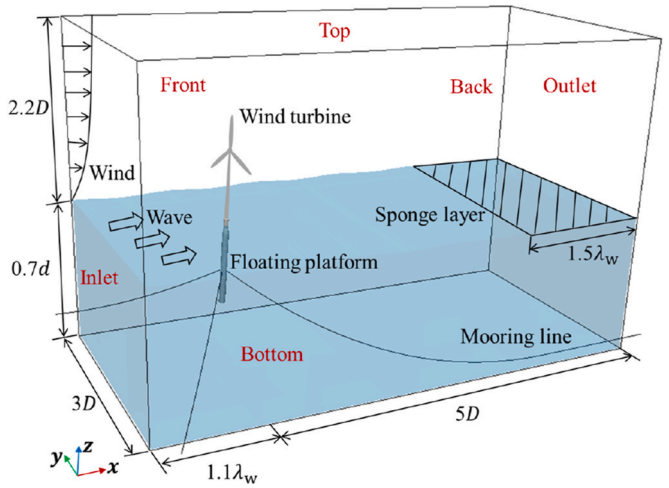

Fig. 7. Computational domain for numerical simulations of the FOWT.

meshes in the computational domain is 5.6 million.

The boundary conditions for the computational domain are defined as follows: At the inlet, the velocity is specified by the incident wind and wave parameters, while a zero-gradient condition is applied at the outlet. Since the bottom boundary does not represent the actual seabed, a slip condition is used, and a pressure outlet condition is applied at the top boundary. For both the front and back boundaries, the normal velocity and pressure gradient are set to zero.

3.3. Wind and wave conditions

A uniform inflow wind condition is selected for the present simulations. For large wind turbines that extend over significant heights, the wind speed varies considerably with altitude. To account for this height-dependent variation, a shear wind profile is employed using an exponential model:

$$u(z) = u_0 \left(\frac{z}{H_0}\right)^{\alpha} \tag{11}$$

where $u(z)$ represents the upstream wind speed at height z, u_0 is the upstream wind speed at hub height H_0, and α is the wind shear exponent. A recommend vale for α is 0.14 for offshore sea conditions (Obhrai et al., 2012). Stokes second-order regular waves are adopted for the incident wave. The directions of the wind and wave are both aligned along the positive x-axis.

In this study, three distinct wind speeds, 5 m/s, 11.4 m/s, and 18 m/s, are evaluated, in conjunction with three sea states as characterized by Jonkman (2010). The specific conditions for numerical simulations are summarized in Table 1, where T_w and A_w denote the wave period and wave amplitude, respectively. The term "CS" refers to GT and BP controllers. Scenarios with the CS "off" mean the FOWT operates with a fixed rotor speed (Ω_R) and a fixed blade pitch angle (θ_p).

All numerical simulations were conducted on the Cirrus UK National Tier-2 HPC Service at EPCC, using standard Cirrus compute nodes. Each node is equipped with two 18-core Intel Xeon E5-2695 (Broadwell) processors operating at 2.1 GHz. Each simulation ran for 300 s on 120 CPUs, with computational times ranging from 66.5 to 86.4 h per case.

3.4. Grid convergence test

Three sets of grids with different mesh resolutions are generated to perform a grid convergence test as provided in Table 2. The upstream wind speed is set to 11.4 m/s, with a corresponding rotor speed of 12.1 rpm, without considering wind shear effects and turbine controllers. To reduce computational time, the FOWT is kept stationary. The time step size used in the simulation is 0.01 s, indicating that the blade rotates by 0.73° at each time step, which is less than the minimum angle requirement for computational convergence mentioned in Tran and Kim's study (Tran and Kim, 2018). This time step also satisfies the Courant-Friedrichs-Lewy (CFL) condition.

Fig. 9 shows the time history of the aerodynamic load coefficients calculated from different mesh resolutions. The discrepancy in the mean values, averaged from 30 s to 50 s, between the medium and fine meshes is 1.5 % for aerodynamic power coefficient (C_P) and 0.9 % for the thrust

Table 1
Simulation conditions for the FOWT.

No.	CS	u_0 (m/s)	Ω_R (rpm)	θ_p (deg)	Sea state	T_w (s)	A_w (s)
Case 1/2	On/Off	11.4	-/12.1	-/0	5	9.7	3.66
Case 3/4	On/Off	5	-/7.49	-/0	5	9.7	3.66
Case 5/6	On/Off	18	-/12.1	-/15	5	9.7	3.66
Case 7/8	On/Off	11.4	-/12.1	-/0	6	11.3	5.49
Case 9/10	On/Off	11.4	-/12.1	-/0	7	13.6	9.14

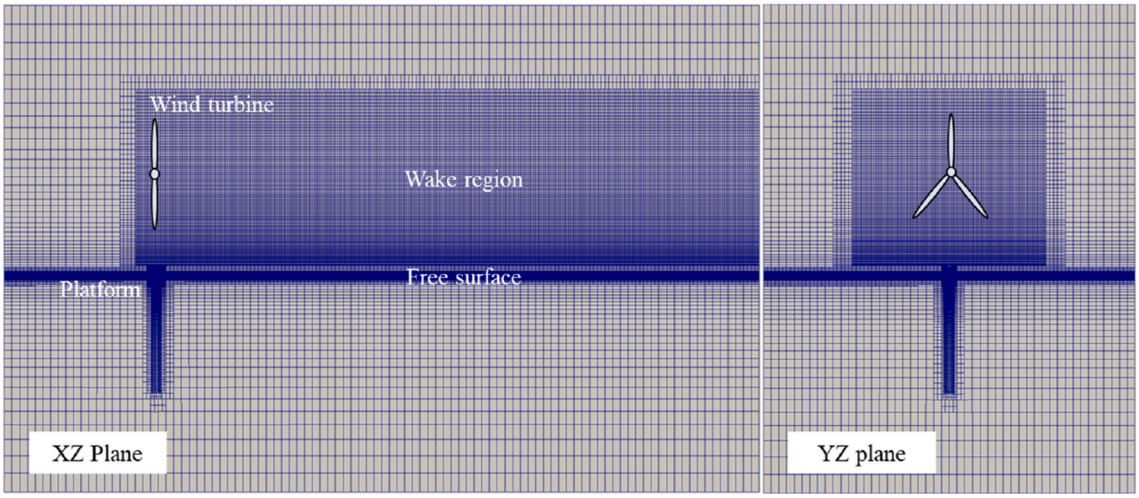

Fig. 8. Grid distribution in the computational domain.

Table 2
Mesh resolution in grid convergence test.

Mesh type	Minimal grid size	Total grid number
Coarse mesh	$2\sqrt{2}$ m $\times 2\sqrt{2}$ m $\times 2\sqrt{2}$ m	2.1 million
Medium mesh	2 m × 2 m × 2 m	5.6 million
Fine mesh	$\sqrt{2}$ m $\times\sqrt{2}$ m $\times\sqrt{2}$ m	14.4 million

coefficient (C_T). As illustrated in Table 3, the discrepancy between the results obtained using the medium mesh and those using the fine mesh does not exceed 1 % for various types of blade tip deformations. Therefore, to enhance computational efficiency while maintaining high accuracy, the medium mesh and a time step of 0.01 s are chosen for the subsequent simulations.

4. Results and discussions

This section presents the coupled dynamic responses of the FOWT using GT and BP controllers across various wind speeds and wave conditions. It examines aerodynamic loads, blade deformation, platform motion, mooring tensions, and wake characteristics to assess the impact of the controllers. Subsection 4.1 focuses on the FOWT's responses under rated wind speed and sea state 5. Subsections 4.2 and 4.3 explore the responses under varying wind speeds and sea states, respectively.

4.1. FOWT responses under rated wind speed and sea state 5

4.1.1. GT and BP controllers' responses

When operating at rated wind speed, the platform motion of the FOWT, particularly surge and pitch motions, leads to significant periodic changes in the inflow wind speed (u_{in}) for the wind turbine, as illustrated in Fig. 10. It should be noted that this speed is measured at a monitoring point located 10 m upstream of the hub centre. The periodic variation in u_{in} results in similar variations in rotor speed (Ω_R) and blade pitch angle (θ_p). With an increase in u_{in}, Ω_R gradually increases under the GT controller. Once Ω_R exceeds the rated value (Ω_0), the BP controller activates, and θ_p begins to increase from 0°. It is noted that u_{in}, Ω_R, and θ_p reach their maximum at different times, designated as t_a, t_b, and t_c, respectively, with $t_a < t_b < t_c$. This indicates that wind turbine control strategies exhibit delays, which could reduce generation efficiency and increase power fluctuations.

To better understand the control processes of GT and BP controllers, we plot the dynamic responses of the rotor and generator, including torque and power, as shown in Fig. 11. These responses exhibit periodic variations that closely match the change period of u_{in}. The control process within one cycle (from t_0 to t_6) is selected for further analysis, as shown in Fig. 12, and is described in detail below.

(a) At t_0, the rotor torque (M_R) and generator torque (M_G) are in equilibrium.
(b) From t_0 to t_1, as u_{in} increases, M_R gradually increases, exceeding M_G. With GT controller, Ω_R continues to increase, causing M_G to gradually increase as well. GT controller is in the region III, as indicated in Fig. 6.
(c) From t_1 to t_2, GT controller enters the region IV, with a rapid increase in M_G.
(d) From t_2 to t_3, as Ω_R further increases beyond the rated speed Ω_0, BP controller is activated, and the blade pitch angle θ_p starts to increase from 0 to reduce Ω_R. Despite the continuous increase in u_{in}, which initially increases M_R, it gradually decreases as θ_p increases. During this period, M_G, under GT controller in the region V, maintains the product of M_G and generator speed Ω_G constant to keep the generator power (P_G) stable, as shown in Fig. 11(b).
(e) At t_3, M_R and M_G reach equilibrium again.
(f) From t_3 to t_4, as u_{in} decreases, the M_R gradually becomes less than M_G, causing Ω_R to gradually decrease, and correspondingly, θ_p also decreases. During this period, M_R remains in the region V of GT controller, and P_G maintains a rated output of 5 MW.
(g) From t_4 to t_5, Ω_R falls below Ω_0, and θ_p gradually returns to 0, subsequently deactivating BP controller. The M_R significantly decreases as u_{in} decreases, and GT controller re-enters the region IV, narrowing the gap between M_R and M_G.
(h) From t_5 to t_6, u_{in} first decreases then increases, and M_R undergoes a process of first decreasing then increasing. Due to the low Ω_R and correspondingly low Ω_G, GT controller remains in the region III.
(i) At t_6, M_R and M_G reach equilibrium again, subsequently initiating the cycle for the next period.

Additionally, a comparison between rotor power (P_R) and P_G is shown in Table 4. Due to generator efficiency factors, the time-averaged P_G is 5.7 % lower than P_R. However, the peak-to-peak amplitude of P_G is 54.5 % lower than P_R. This highlights the critical role of control strategies in significantly reducing variations in the generator's power output, thereby enhancing power generation quality.

In summary, the GT controller remains continuously active. When the inflow wind speed is below the rated value, the GT controller increases the rotor speed to boost power output. Conversely, when the wind speed exceeds the rated value, the BP controller is activated in

Table 3
Blade tip deformation in grid convergence test.

Mesh type	Flap-wise deformation δ_0 (m)	Edgewise deformation δ_1 (m)	Torsional deformation δ_θ (deg)
Coarse mesh	3.680	0.470	3.056
Medium mesh	3.792	0.493	3.080
Fine mesh	3.800	0.496	3.083

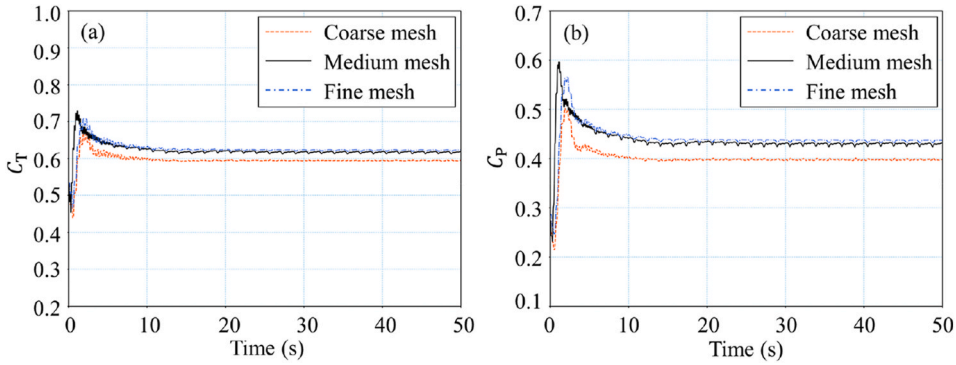

Fig. 9. Aerodynamic load coefficients of the FOWT in grid convergence test: (a) C_T; (b) C_P.

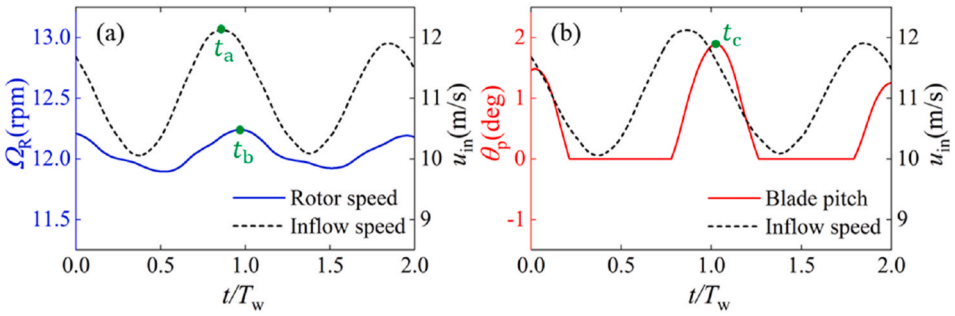

Fig. 10. Dynamic responses of the wind turbine controllers: (a) Ω_R; (b) θ_p.

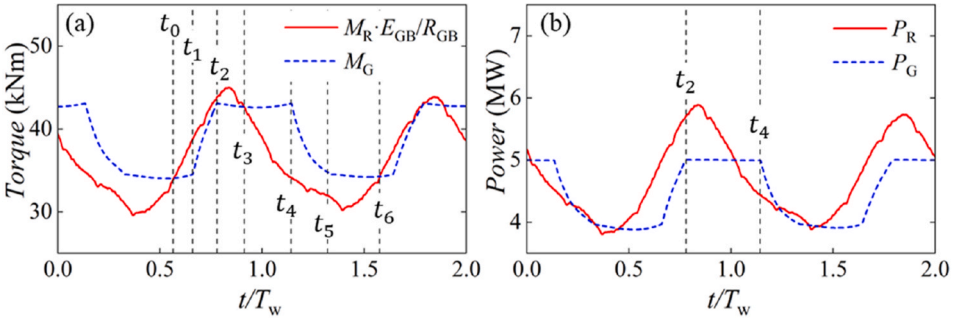

Fig. 11. Dynamic responses of the rotor and generator: (a) torque; (b) power.

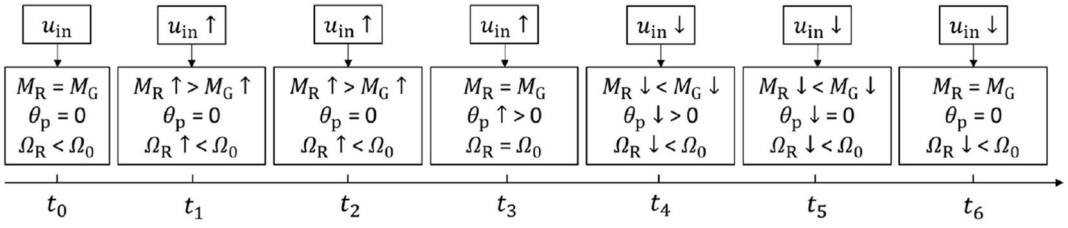

Fig. 12. Dynamic responses of GT and BP controllers.

Table 4
Power output of the rotor and generator of the FOWT with the CS.

Device	Time-averaged value (MW)	Peak-to-peak amplitude (MW)
Rotor	4.76	2.46
Generator	4.49	1.12

conjunction with the GT controller to maintain rated power. By increasing the blade pitch angle, the BP controller reduces the aerodynamic load, thereby ensuring stable power generation.

4.1.2. Aeroelastic responses

When GT and BP controllers are activated in FOWT operations, Ω_R and θ_p are adjusted in response to inflow conditions. As indicated by Eqs. (A.3) ~ (A.5), these adjustments alter the angle of attack (α), influencing the aerodynamic loads. Fig. 13 compares the α of blade #1 with and without the CS, showing a notable reduction in the variation amplitude of α with the CS. For the blade section at $x/R = 0.8$, the root mean square (RMS) and standard deviation (STD) of α decrease by 6.8 % and 29.8 %, respectively.

As depicted in Fig. 14, the aerodynamic loads exhibit periodic variations with significant amplitudes due to the 6DoF motions of the

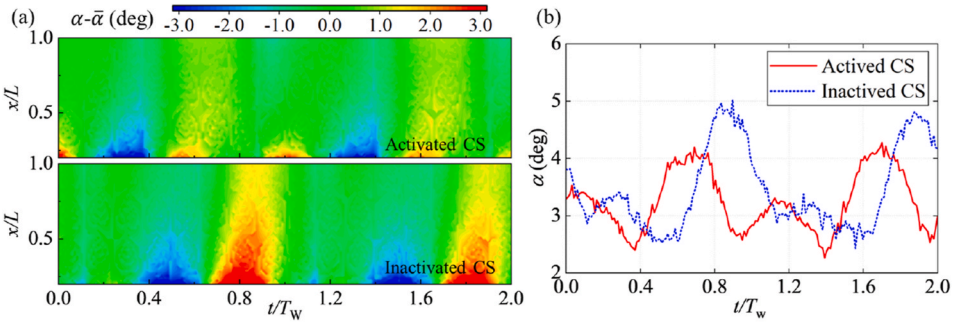

Fig. 13. Angle of attack (α) of the blade #1 of FOWT: (a) distribution of α along the blade length direction; (b) α at $x/R = 0.8$ ($R = 63$m is the rotor radius).

floating platform. With the CS activated, C_P notably decreases during 0.8 T_w ~1.2 T_w when the BP controller is engaged. The reduction in C_T is more pronounced than in C_P. As summarized in Table 5, the RMS values of C_P and C_T decrease by 1.8 % and 3.4 %, respectively, while the STD of C_P and C_T significantly decrease by 15.3 % and 19.6 %, indicating improved aerodynamic load stability. Additionally, the decrease in aerodynamic thrust due to the tower shadow effect is highlighted in Fig. 14(b) with black dashed circles.

Changes in aerodynamic loads from the activated CS further induce variations in blade-root bending moments. Fig. 15 illustrates the out-of-plane moment (M_{oop}), low-speed-axis moment (M_{lsa}) of blade #1, and the yaw moment (M_{yaw}) of the FOWT, assessing the CS's impact on fatigue loading (M_{oop} and M_{lsa}) of the wind turbine. Similar to aerodynamic loads, M_{oop} and M_{lsa} exhibit periodic variations closely aligning with the wave period. Compared to scenarios with an inactivated CS, M_{oop} and M_{lsa} under an activated CS display more complex variations and reduced maximum values.

As indicated in Table 5, the RMS of M_{oop} and M_{lsa} decrease by 3.3 % and 1.6 %, respectively, and the STD by 9.7 % and 25.1 %. This suggests the CS significantly reduces fatigue loading. M_{yaw} also exhibits periodic variations, with two dominant frequencies, i.e., one corresponding to the wave period and the other to the blade's rotational period. The impact of the CS on M_{yaw} is less pronounced than on M_{lsa}, yet it still contributes to a reduction. The RMS and STD of M_{yaw} decrease by 1.6 % and 9.2 % with the activated CS.

Variations in aerodynamic loads also influence the structural deformation of wind turbine blades. Fig. 16 presents a detailed comparative analysis of the temporal and spatial distributions of structural deformations in blade #1, including the time history of blade tip displacements. Table 6 summarizes the RMS and STD values of blade tip deformation, comparing conditions with and without the CS. The RMS values for all types of blade deformations, including flap-wise (δ_0), edgewise (δ_1), and torsional (δ_θ), decrease when the CS is activated, with the most notable reduction observed in δ_1. The STD values for δ_0 and δ_1 also significantly decrease, with the reduction magnitude surpassing that of the RMS values, indicating that the CS notably reduces structural deformations. However, the STD of δ_θ significantly increases, primarily due to the BP controller inducing a wider range of variations in θ_p, subsequently amplifying the rotational moment acting on the blade.

4.1.3. Hydrodynamic responses

In the FOWT system, the interaction between the wind turbine and the floating platform allows the CS to indirectly influence 6DoF motions by altering aerodynamic loads. Given the alignment of wind and wave directions along the positive x-axis and the platform's geometric symmetry, sway and roll motions are minimal. Therefore, our analysis focuses on the platform's surge, heave, pitch, and yaw motions, as depicted in Fig. 17. Previous studies have shown that both aerodynamic and hydrodynamic loads predominantly influence the time-mean values and variation amplitudes of platform motions, respectively (Huang and Wan, 2019). With the activated CS, the mean surge displacement decreases by 5.1 % due to reduced aerodynamic thrust, leading to a smaller time-mean pitch angle. The variation in platform pitch motion increases, enhancing the aerodynamic force in the z-axis direction and increasing heave motion amplitude. Additionally, the increased yaw moment amplitude from the wind turbine leads to a larger yaw motion amplitude.

Table 5
Statistical values of aerodynamic load coefficients and root bending moments.

	CS	C_P (−)	C_T (−)	M_{oop} (10^6 Nm)	M_{lsa} (10^6 Nm)	M_{yaw} (10^6 Nm)
RMS	On	0.4526	0.6404	7.879	1.262	0.313
	Off	0.4613	0.6583	8.151	1.282	0.318
STD	On	0.06652	0.04460	0.607	0.176	0.079
	Off	0.07273	0.05152	0.668	0.235	0.087

The influence of the CS on the hydrodynamic responses is further examined by investigating mooring forces. Fig. 18 displays the mooring forces of lines #1 and #2, with lines #2 and #3 symmetrically distributed along the x-axis and exhibiting similar forces. Initially, all mooring lines are subjected to identical pretension forces. As the platform's surge displacement increases, the mooring force of line #1 decreases, while that of line #2 increases. With the activated CS, the mean surge displacement is reduced, leading to an increase in the mooring force for line #1 and a decrease for line #2.

4.1.4. Wake development and visualization

To examine the impact of the CS on wake development and flow field characteristics, we analyse the instantaneous vortex structure, wake velocity (u_w), and turbulence intensity (TI) as shown in Fig. 19 The wake vortex, visualized using the Q-criterion and coloured by wake velocity, is displayed along with the free surface based on wave elevation. Distinct vortex rings are observed at both the blade root and tip. As the vortex ring propagates downstream, the vortices expand and merge into larger structures. The vortex structure forms an acute angle (θ_v) relative to the horizontal plane, as highlighted in Fig. 20. It is observed that the CS causes earlier merging of vortex rings within a shorter downstream distance and reduces θ_v. This indicates that the wake vortex is more prone to expansion upon interacting with the free surface, increasing wake instability.

Furthermore, we present the time-averaged wake velocity deficit ($\overline{u}_d$) and turbulence intensity at the hub-height horizontal plane, as depicted in Figs. 21 and 22. The wake velocity deficit (u_d) is defined as follows:

$$u_d = (u_{in} - u_w) / u_{in} \tag{12}$$

Compared to the scenario without the CS, $\overline{u}_d$ significantly decreases beyond $x/L = 3D$, as indicated by the black dashed circles. This region also shows a notable increase in TI. These findings indicate that the control system not only increases the wake velocity but also creates an unstable wake field that aids in wake recovery. However, this may worsen the inflow conditions for downstream wind turbines by

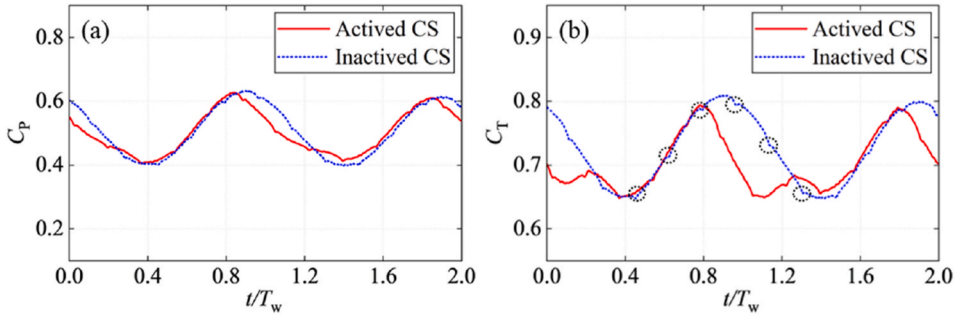

Fig. 14. Aerodynamic load coefficients of FOWT with and without wind turbine control: (a) C_P; (b) C_T.

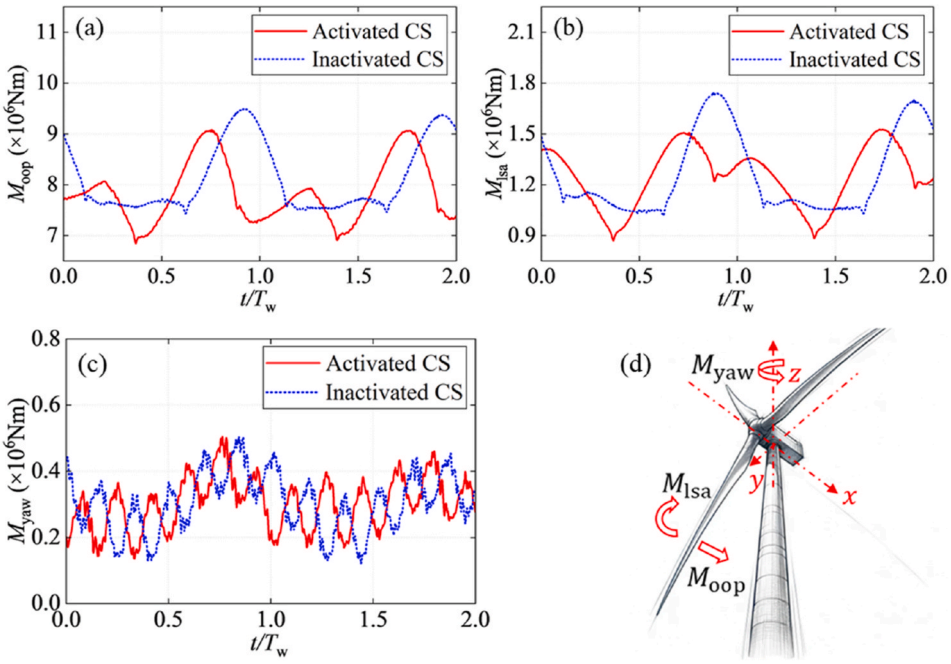

Fig. 15. Dynamic responses of blade-root bending moments and the yaw moment of FOWT: (a) M_{oop}; (b) M_{lsa}; (c) M_{yaw}; (d) schematic diagram of different moments.

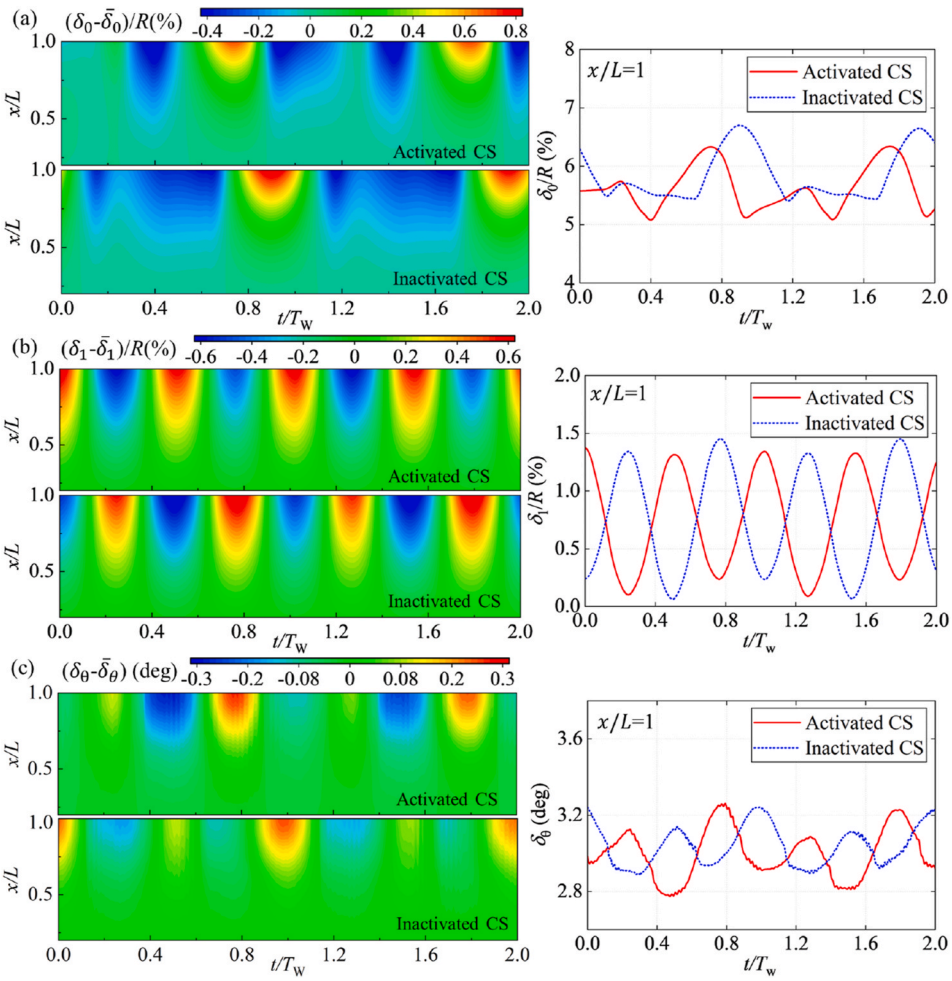

Fig. 16. Time and spatial distribution of the structural deformation of blade #1: (a) δ_0; (b) δ_1; (c) δ_θ.

Table 6
Statistical values of the tip displacements of blade #1.

CS	δ_0 (m)		δ_1 (m)		δ_θ (deg)	
	RMS	STD	RMS	STD	RMS	STD
On	3.555	0.237	0.523	0.258	3.000	0.131
Off	3.692	0.266	0.561	0.278	3.039	0.105
Discrepancy (%)	−3.7 %	−10.9 %	−6.8 %	−7.2 %	−1.3 %	24.8 %

increasing turbulence intensity, which makes power output more unstable. Therefore, in floating wind farm layouts, downstream turbines should be positioned to avoid the near-wake region of upstream turbines.

4.2. FOWT responses at varying wind speeds

4.2.1. Rotor speed and blade pitch angle

Fig. 23 illustrates the dynamic responses of the controllers, specifically Ω_R and θ_p. At an upstream wind speed (u_0) of 5 m/s, the 6DoF motions of the floating platform induce periodic variations in u_{in}, but the magnitude remains below the rated value, activating only the GT controller. Consequently, Ω_R varies periodically to maximize power output, while θ_p remains at 0°. At $u_0 = 11.4$ m/s, u_{in} varies near the rated wind speed due to the platform motions, activating both GT and BP controllers. Here, Ω_R shows greater variability compared to when u_0 is 5 m/s, and θ_p occasionally exceeds 0° to ensure the FOWT's power output does not exceed the rated capacity. When u_0 increases to 18 m/s, u_{in} consistently exceeds the rated wind speed. Ω_R changes periodically around the rated rotational speed of 12.1 rpm, and θ_p also undergoes periodic changes, allowing the FOWT to operate stably at rated power.

4.2.2. Aerodynamic load

The ratios of aerodynamic loads of the FOWT with and without the CS are calculated by Eq. (13).

$$R_p = C_P / C_P', R_T = C_T / C_T' \tag{13}$$

where R_p and R_T represent the ratios of C_P and C_T, respectively. Variables marked with a ' denote scenarios without the CS, while unmarked variables indicate scenarios with the CS. This notation is used consistently in Eq. (14) ~ (17).

As illustrated in Fig. 24, as u_0 increases from 5 m/s to 18 m/s, the RMS values of R_p and R_T gradually increase, while their corresponding STD values consistently decrease. This indicates that the impact of the CS on the FOWT's aerodynamic loads becomes more pronounced with increasing wind speed. At u_0 = 5 m/s and 11.4 m/s, where the GT controller predominates, both the RMS and STD of R_p and R_T are <1, with STD values lower than RMS values. This suggests that the CS reduces the mean aerodynamic loads and significantly decreases the

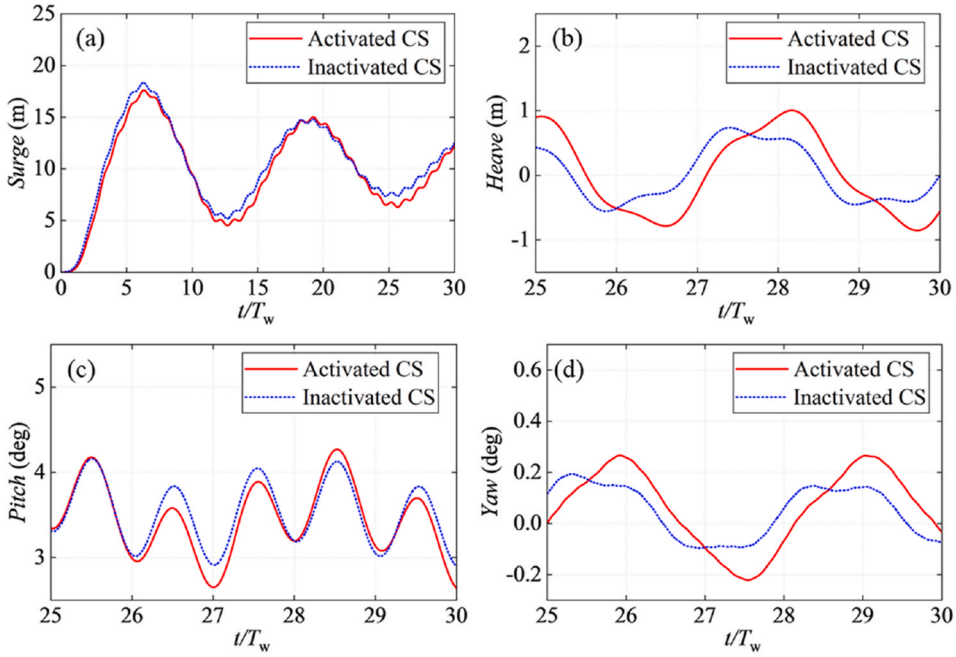

Fig. 17. Time history curves of platform motions: (a) surge; (b) heave; (c) pitch; (d) yaw.

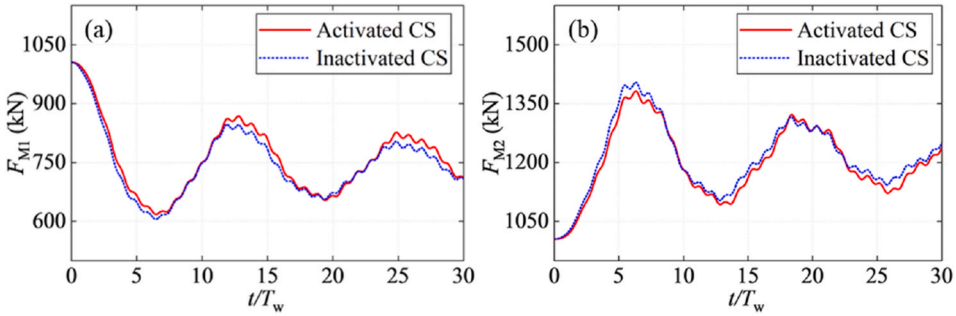

Fig. 18. Time history curves of mooring forces: (a) mooring line #1; (b) mooring line #2.

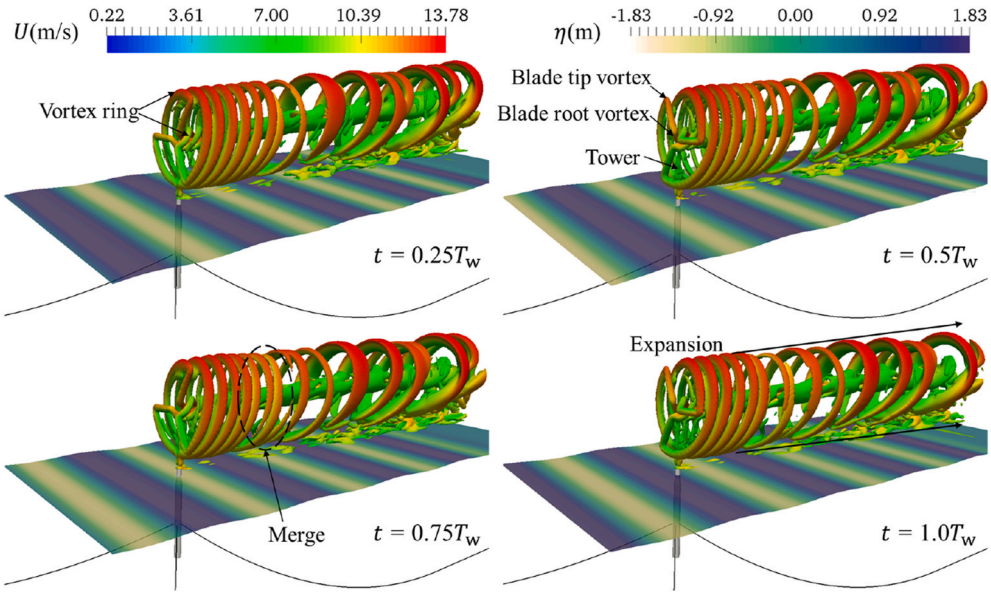

Fig. 19. Four instants of the wake vortex of the FOWT within one wave period.

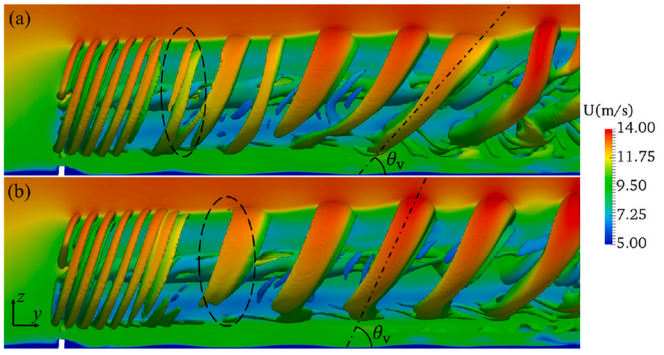

Fig. 20. Comparison of the wake vortex of the FOWT: (a) activated CS; (b) inactivated CS.

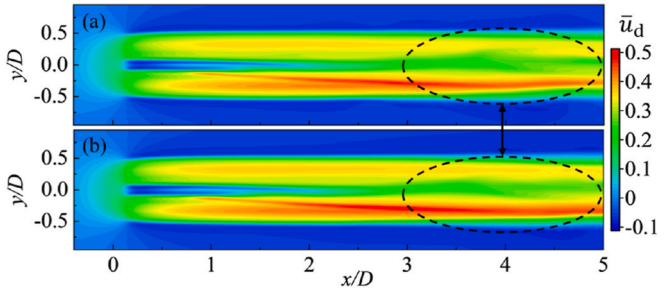

Fig. 21. Wake velocity deficit distribution in the hub-height horizontal plane: (a) activated CS; (b) inactivated CS.

amplitude of load variations, which stabilizes power output and enhances electricity generation quality. At $u_0 = 18$ m/s, where the BP controller assumes a dominant role, both the RMS of R_p and R_T exceed 1, and the STD are less than 1. This demonstrates that the CS significantly increases the average power output of FOWTs while markedly reducing load variation amplitude, underscoring the CS's crucial role at high wind speeds.

To assess the CS's effect on blade fatigue loading at various wind speeds, we compute the ratios of M_{oop}, M_{lsa}, and M_{yaw} for the FOWT with and without the CS, as defined by Eq. (14) and illustrated in Fig. 25.

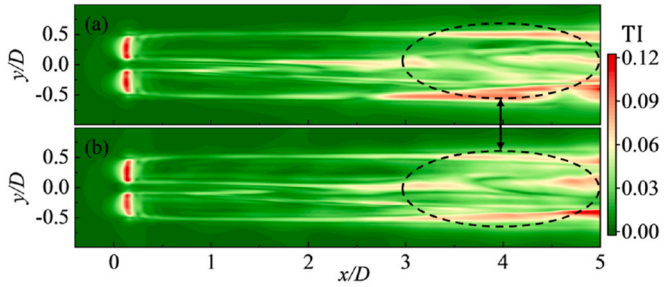

Fig. 22. Turbulence intensity distribution in the hub-height horizontal plane: (a) activated CS; (b) inactivated CS.

$$R_{Moop} = M_{oop}/M_{oop}', R_{Mlsa} = M_{lsa}/M_{lsa}', R_{yaw} = M_{yaw}/M_{yaw}' \quad (14)$$

Observations reveal that the CS's impact on M_{oop} and M_{lsa} mirrors its influence on aerodynamic loads, intensifying as wind speed increases. At $u_0 = 5$ m/s and 11.4 m/s, the CS slightly reduces the RMS and STD of M_{oop} and M_{lsa}, though the overall impact is not significant. Conversely, at $u_0 = 18$ m/s, there is a substantial increase in the RMS values of M_{oop} and M_{lsa} and a significant reduction in their STD values. These findings suggest that the CS plays a crucial role in reducing the variation amplitude of M_{oop} and M_{lsa} at elevated wind speeds, thus mitigating fatigue loading. Similarly, the CS's impact on M_{yaw} becomes more pronounced as u_0 increase, consistently reducing both its RMS and STD values.

4.2.3. Blade deformation

As defined in Eq. (15), we calculate the ratios of blade tip deformation for the FOWT with and without the CS. The findings are presented in Fig. 26.

$$R_{\delta 0} = \delta_0/\delta_0', R_{\delta 1} = \delta_1/\delta_1', R_{\delta\theta} = \delta_\theta/\delta_\theta' \quad (15)$$

At $u_0 = 5$ m/s and 11.4 m/s, the CS minimally affects the blade deformation, with reductions in both the RMS and STD of δ_0 and δ_1 not exceeding 5 %. For δ_θ, the RMS reduction is below 5 %, but the STD increases by 25 % and 32 % at 5 m/s and 11.4 m/s, respectively, indicating a significant enhancement in the variation amplitude of δ_θ.

At $u_0 = 18$ m/s, due to increased blade-root bending moments, there

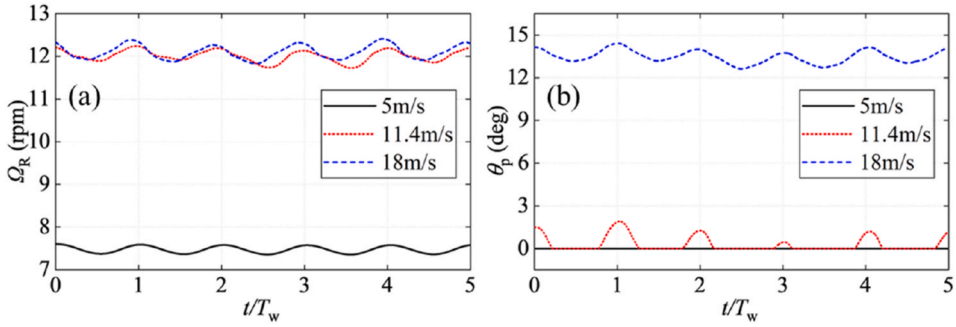

Fig. 23. Dynamic responses of the CS at varying wind speeds: (a) Ω_R; (b) θ_p.

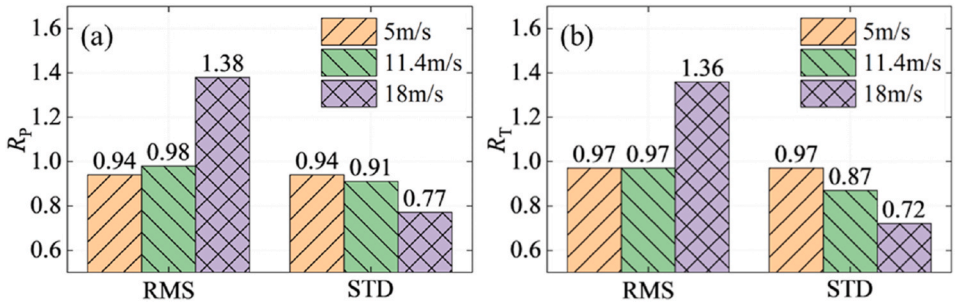

Fig. 24. Ratios of aerodynamic loads with and without the CS: (a) R_P; (b) R_T.

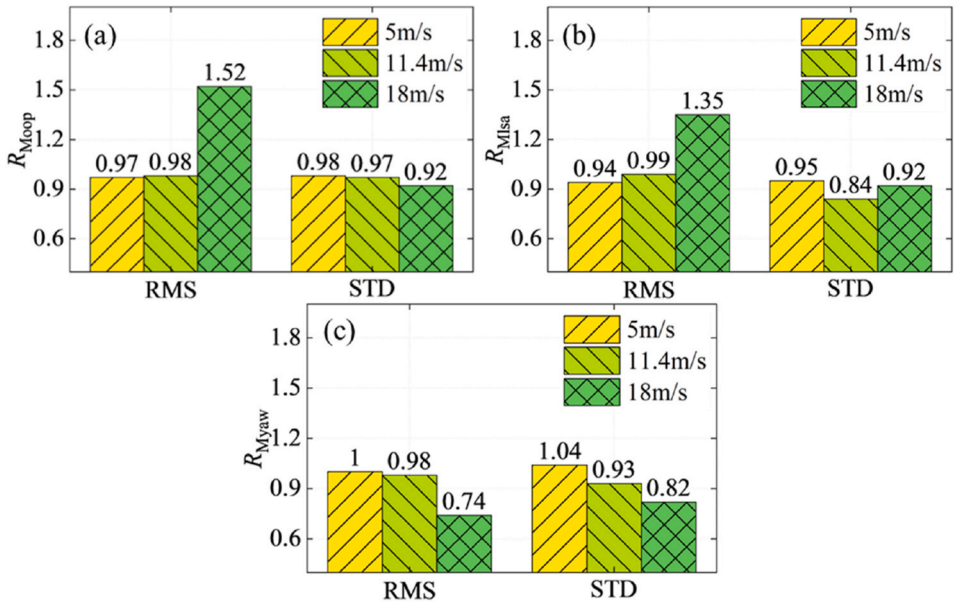

Fig. 25. Ratios of blade-root bending moments and the yaw moment with and without the CS: (a) R_{Moop}; (b) R_{Mlsa}; (c) and R_{Myaw}.

is a marked rise in the RMS of blade deformation, with increases of 79 %, 14 %, and 5 % in δ_0, δ_1, and δ_θ, respectively. Changes in STD are also pronounced, with a 29 % reduction in δ_0 and a 20 % increase in δ_θ. These observations highlight the complex effects of the CS on blade deformation at different wind speeds. In summary, the CS increases the amplitude of δ_θ at various wind speeds, with this effect becoming more pronounced at higher wind speeds.

4.2.4. Platform motion

Using Eq. (16), we calculate the ratios of platform motions with and without the CS:

$$R_{surge} = d_x/d_x', R_{heave} = d_z/d_z', R_{pitch} = \theta_{ry}/\theta_{ry}', R_{yaw} = \theta_{rz}/\theta_{rz}' \quad (16)$$

where d_x, d_z, θ_{ry}, and θ_{rz} represent the surge displacement, heave displacement, platform pitch angle, and platform yaw angle, respectively. As shown in Fig. 27, at $u_0 = 18$ m/s, the CS significantly enhances both the mean values and amplitudes of platform motion responses due to increased aerodynamic thrust. At $u_0 = 11.4$ m/s, it notably increases the amplitudes of heave and yaw motions, while its effect on surge and pitch is less pronounced. At $u_0 = 5$ m/s, the influence of the CS on platform motions is minimal, indicating negligible impact.

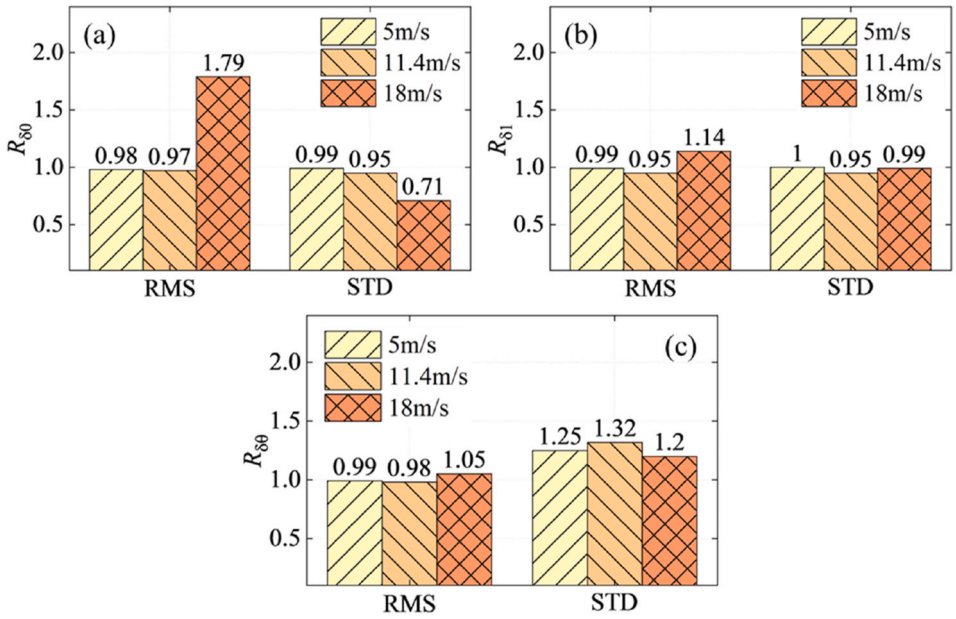

Fig. 26. Ratios of blade tip deformations with and without the CS: (a) $R_{\delta 0}$; (b) $R_{\delta 1}$; (c) $R_{\delta \theta}$.

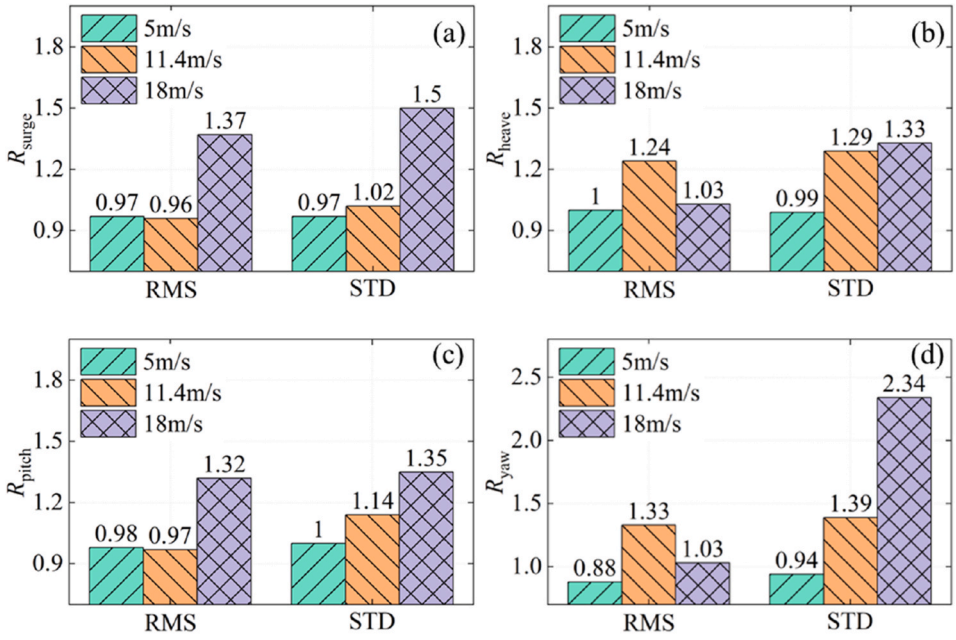

Fig. 27. Ratios of platform motions with and without the CS: (a) R_{surge}; (b) R_{heave}; (c) R_{pitch}; (d) R_{yaw}.

4.2.5. Wake field

To compare the CS's effects on wake characteristics at various wind speeds, the ratios of time-averaged wake velocity ($\overline{u}_w$) and turbulence intensity (TI) with and without the CS are calculated by Eq. (17). Figs. 28 and 29 show the distribution of results within the horizontal plane at hub height ($z = 90$ m), with black solid lines delineating regions where $R_{Uw} = R_{TI} = 1$.

$$R_{Uw} = u_w / u_w', R_{TI} = TI / TI' \tag{17}$$

As depicted in Fig. 28(a) and (b), at $u_0 = 5$ m/s and 11.4 m/s, incorporating the CS increases $\overline{u}_w$. This increase is due to the CS reducing aerodynamic loads on the wind turbine, thereby diminishing the wind energy captured by the FOWT. Conversely, at $u_0 = 18$ m/s, the CS increases the aerodynamic loads, significantly reducing $\overline{u}_w$, as shown in Fig. 28(c). Additionally, in the near-wake region ($x/D < 3$), the CS causes a greater increase in $\overline{u}_w$ at $u_0 = 5$ m/s compared to $u_0 = 11.4$ m/s. However, this trend reverses beyond $x/D = 3$.

Similar to its effects on $\overline{u}_w$, the CS increases TI in the wake field at $u_0 = 5$ m/s and 11.4 m/s, increasing flow field instability. Conversely, at $u_0 = 18$ m/s, it significantly reduces TI, decreasing flow field instability. Additionally, at $u_0 = 11.4$ m/s, the CS causes a more pronounced increase in TI compared to $u_0 = 5$ m/s, indicating greater flow field instability under this condition.

4.3. FOWT responses under different sea states

4.3.1. Rotor speed and blade pitch angle

As outlined in Table 1, this study considers three sea states (5, 6, and

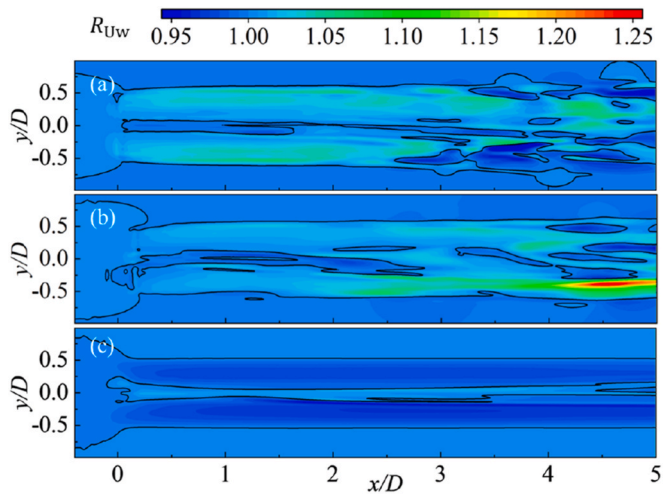

Fig. 28. Wake velocity distribution in the hub-height horizontal plane: (a) 5 m/s; (b) 11.4 m/s; (c) 18 m/s.

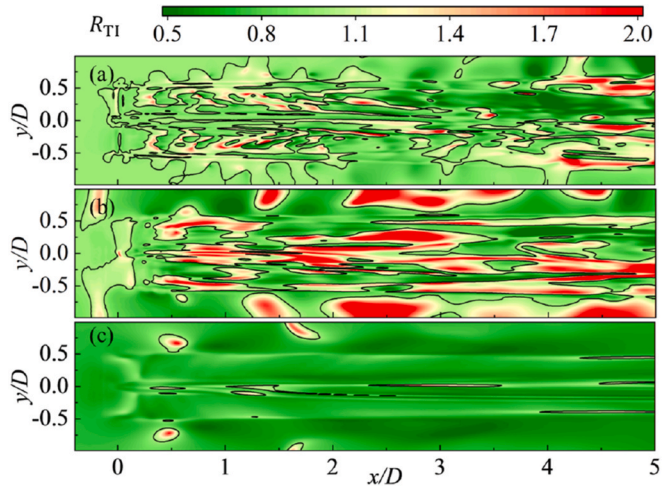

Fig. 29. Turbulence intensity distribution in the hub-height horizontal plane: (a) 5 m/s; (b) 11.4 m/s; (c) 18 m/s.

7). With increasing sea state levels, both A_w and T_w notably increase. Previous studies (Tran and Kim, 2015a, 2015b; Huang and Wan, 2019) suggest that higher A_w enhance the amplitude of 6DoF motions, increasing the variation in u_{in} for FOWTs. This, in turn, leads to more pronounced variations in Ω_R and θ_p, as shown in Fig. 30. Additionally, as A_w increases, the time-averaged Ω_R decreases, while the time-averaged θ_p significantly increases.

4.3.2. Aerodynamic load

As shown in Fig. 31, we compare the aerodynamic loads of the FOWT under different sea states. Ratios of aerodynamic loads with and without the CS are quantified according to Eq. (13). Analysis indicates that the CS significantly reduces the RMS and STD of the aerodynamic loads under different sea states, with a greater reduction in STD than RMS. This signifies that while the average aerodynamic power decreases, there is a more significant reduction in the variation amplitude, thus enhancing power generation stability. Additionally, an increase in A_w results in a progressive decrease in both the RMS and STD of R_p and R_t, demonstrating a more pronounced effect of the CS on the aerodynamic loads.

The ratios of M_{oop}, M_{lsa}, and M_{yaw} for the FOWT with and without the CS are calculated using Eq. (14) and depicted in Fig. 32. Across all sea states, the CS reduces the RMS and STD of M_{oop}, M_{lsa}, and M_{yaw}, with a more substantial reduction in STD than RMS, mitigating blade fatigue loads. The CS's impact is most pronounced on M_{oop} for RMS across different sea conditions, while the greatest reduction in STD is observed in M_{lsa}. Additionally, as A_w increases, the RMS and STD of R_{Moop}, R_{Mlsa}, and R_{yaw} gradually decrease, indicating an amplified effect of the CS.

4.3.3. Blade deformation

Fig. 33 illustrates the impact of the CS on the blade deformation across various sea states. The ratios of δ_0, δ_1, and δ_0 with and without the CS are calculated by Eq. (15). For δ_0, as A_w increases, the CS gradually decreases RMS but increases STD, indicating a stronger effect on δ_0. The impact on δ_1 is less pronounced; the CS reduces both RMS and STD by no more than 5 % across sea states, except for a 14 % RMS decrease at sea state 7. For δ_0, the RMS decrease is modest, not exceeding 7 % across sea states. However, the STD increases by over 30 % with the CS, primarily due to significant variations in θ_p leading to increased aerodynamic torque amplitude.

4.3.4. Platform motion

The ratios of platform motions with and without the CS are calculated using Eq. (16), with results presented in Fig. 34. At sea state 5, the CS increases the mean values and variation amplitudes of heave and yaw responses, while reducing the mean values of surge and pitch motions but increasing their variation amplitudes. At sea state 6, the CS's amplifying effect on platform motions diminishes. At sea state 7, the CS significantly suppresses platform motions via markedly reducing both mean values and variation amplitudes. Overall, the CS decreases the mean values of surge and pitch motions, with this effect becoming more pronounced at higher sea states. The amplifying effect on platform heave and yaw motions decreases as the sea state level increases.

4.3.5. Wake field

The ratio of $\overline{u}_w$ with and without the CS is calculated using Eq. (17), and its distribution at hub height ($z = 90$ m) is shown in Fig. 35. The black solid lines denote where $R_{Uw} = 1$. The inclusion of the CS leads to a marked increase in $\overline{u}_w$ behind the FOWT, corresponding to the reduced

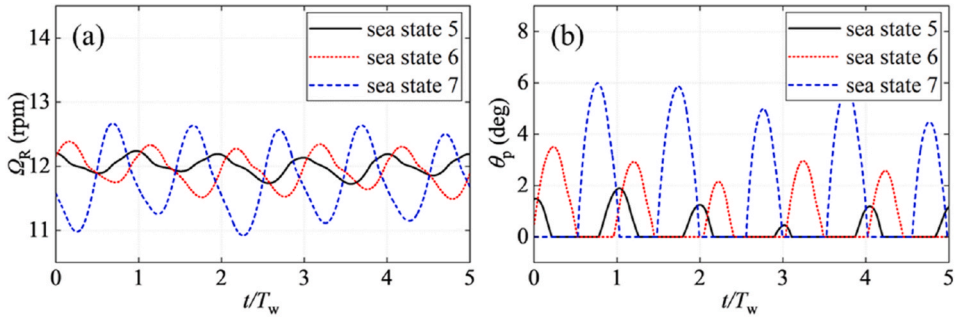

Fig. 30. Dynamic responses of the CS under different sea states: (a) Ω_R; (b) θ_p.

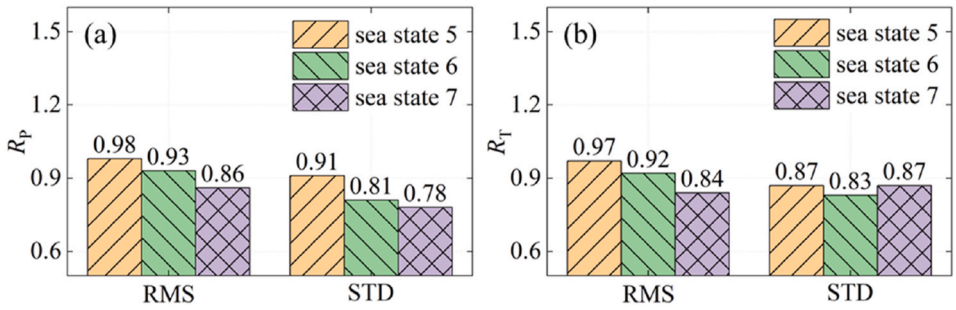

Fig. 31. Ratios of aerodynamic loads with and without the CS: (a) R_p; (b) R_t.

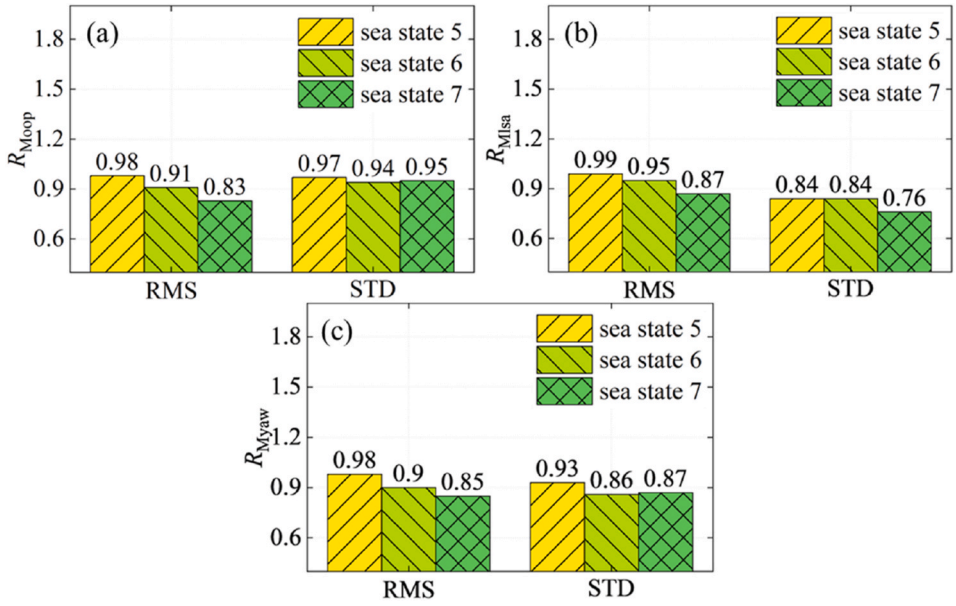

Fig. 32. Ratios of blade-root bending moments and the yaw moment with and without the CS: (a) R_{Moop}; (b) R_{Mlsa}; (c) and R_{Myaw}.

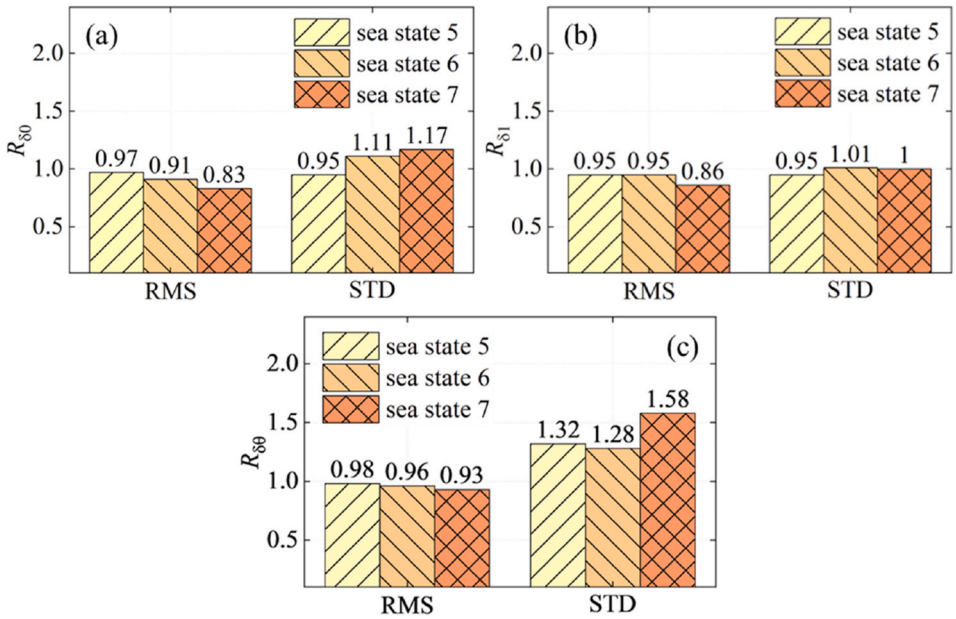

Fig. 33. Ratios of blade tip deformations with and without the CS: (a) $R_{\delta 0}$; (b) $R_{\delta 1}$; (c) $R_{\delta \theta}$.

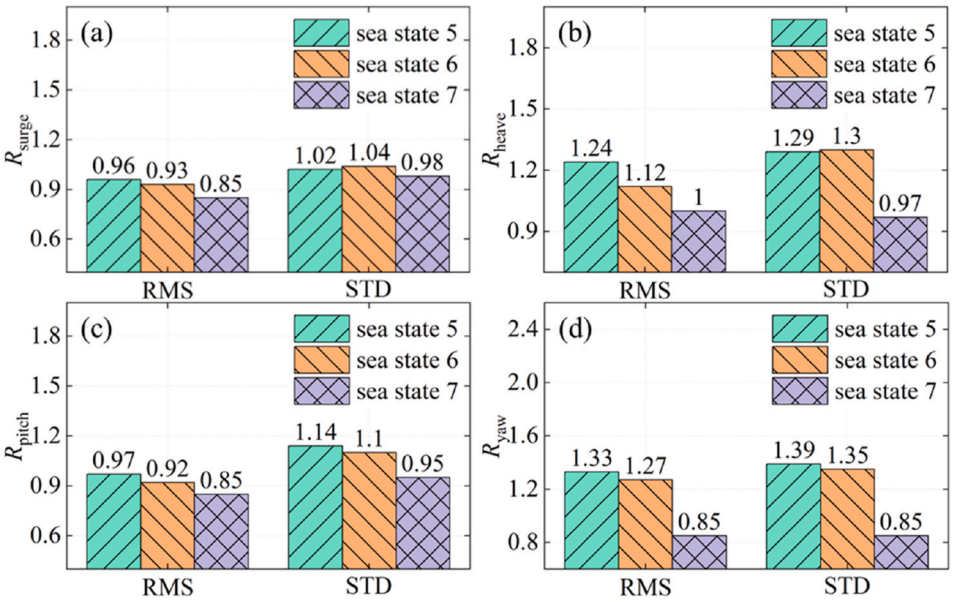

Fig. 34. Ratios of platform motions with and without the CS: (a) R_{surge}; (b) R_{heave}; (c) R_{pitch}; (d) R_{yaw}.

aerodynamic loads when the CS is activated. This increase in $\overline{u}_w$ is due to the FOWT extracting less wind energy from the incoming flow. Furthermore, as A_w increases, R_{Uw} rises significantly, indicating that the CS's effect on improving wake velocity becomes more pronounced.

Furthermore, the distribution of TI in the FOWT's wake with and without the CS across various sea states is depicted in Fig. 36. For sea states 5 and 6, the TI behind the FOWT markedly increases, indicating that the CS significantly enhances wake field instability, potentially deteriorating inflow conditions for downstream turbines. However, in sea state 7, TI increases in the vicinity of wind turbine ($x/D < 2$) but decreases farther away ($x/D > 2$).

5. Conclusions

In this study, a fully coupled analysis tool integrating aerodynamics, hydrodynamics, blade elasticity, mooring lines, and control system is employed to perform numerical simulations of a spar-type FOWT equipped with GT and BP controllers across various wind speeds and sea states. The dynamic behaviours of the FOWT, including controller responses, aerodynamic loads, blade deformations, platform motions, mooring line tensions, and wake dynamics, is extensively examined to explore the impact of GT and BP controllers on FOWT performance. Several conclusions can be drawn from our numerical results.

GT and BP controllers effectively reduce the variation amplitudes of aerodynamic loads on the FOWT across different wind and wave conditions. As u_0 or A_w increases, the CS progressively enhances the reduction of the STD of aerodynamic loads, including C_P and C_T, indicating a growing influence on aerodynamic performance. Notably, the CS markedly increases the RMS of aerodynamic loads when u_0 exceeds the rated speed, while it reduces them in other scenarios, underscoring its importance at high wind speeds. The CS's impact on M_{oop} and M_{lsa} mirrors its effect on C_T and C_P. For M_{yaw}, both the STD and RMS values decrease as u_0 and A_w increase. Regarding platform motions, the CS significantly increases both the mean values and variation amplitudes at $u_0 = 18$ m/s, while at sea state 7, it substantially suppresses platform motions. Additionally, the wake field undergoes significant alterations due to the CS, with changes in u_w inversely related to changes in the RMS of C_P. Specifically, an increase in C_P induced by the CS leads to a reduction in u_w. Except at $u_0 = 18$ m/s, the CS amplifies TI in the wake, particularly in the near wake region ($x/D < 3$), significantly increasing

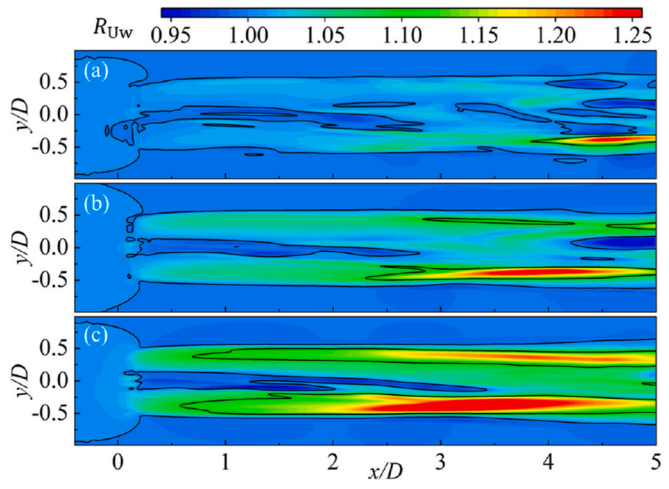

Fig. 35. Wake velocity distribution in the hub-height horizontal plane: (a) sea state 5; (b) sea state 6; (c) sea state 7.

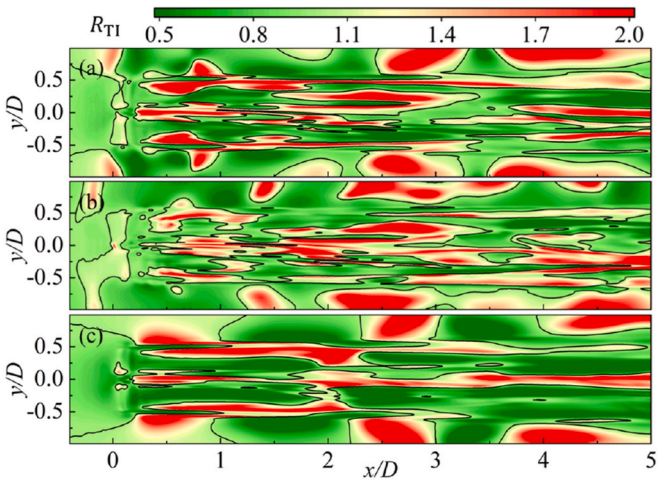

Fig. 36. Turbulence intensity distribution in the hub-height horizontal plane: (a) sea state 5; (b) sea state 6; (c) sea state 7.

flow field instability across various wind speeds and sea states.

The present work enhances our understanding of the dynamic responses of FOWTs equipped with GT and BP controllers, providing insights into how the control system influences FOWT performance. However, our analysis is limited to wind turbine control systems and does not consider platform control strategies, such as station-keeping and motion damping. Additionally, only scenarios involving regular waves and uniform wind inflow are analysed. Future research will investigate the impact of platform control systems on FOWT dynamic responses and incorporate irregular waves and atmospheric boundary layer conditions to achieve a more comprehensive understanding of FOWT behaviours in realistic marine environments.

CRediT authorship contribution statement

Yang Huang: Writing – review & editing, Writing – original draft, Visualization, Validation, Software, Methodology, Investigation, Formal analysis, Data curation, Conceptualization. **Qing Xiao:** Writing – review & editing, Writing – original draft, Validation, Supervision, Resources, Methodology, Investigation, Formal analysis, Conceptualization. **Decheng Wan:** Writing – review & editing, Supervision, Software, Resources, Investigation, Formal analysis, Conceptualization.

Declaration of competing interest

The authors declare that they have no known competing financial interests or personal relationships that could have appeared to influence the work reported in this paper.

Acknowledgements

This work used the Cirrus UK National Tier-2 HPC Service at EPCC (http://cirrus.ac.uk) funded by the University of Edinburgh and EPSRC (EP/P020267/1).

Appendix A. Aerodynamic model

Due to its efficiency and relatively low computational cost, the ALM (Troldborg, 2009) is employed to predict the aerodynamic performance of wind turbines in this study. In this model, the blades are represented by actuator lines, discretized into a series of actuator points. The aerodynamic forces on the blades are calculated based on blade element momentum theory (Manwell et al., 2010) and distributed across the actuator points. These forces are projected into the flow field using a Gaussian kernel function (Gao and Wang, 2020) to replicate the turbine wake. However, the ALM is initially developed for fixed wind turbines and does not account for the 6DoF motions of the floating platform or the structural deformation of wind turbine blades. To address this, modifications are made to the original ALM.

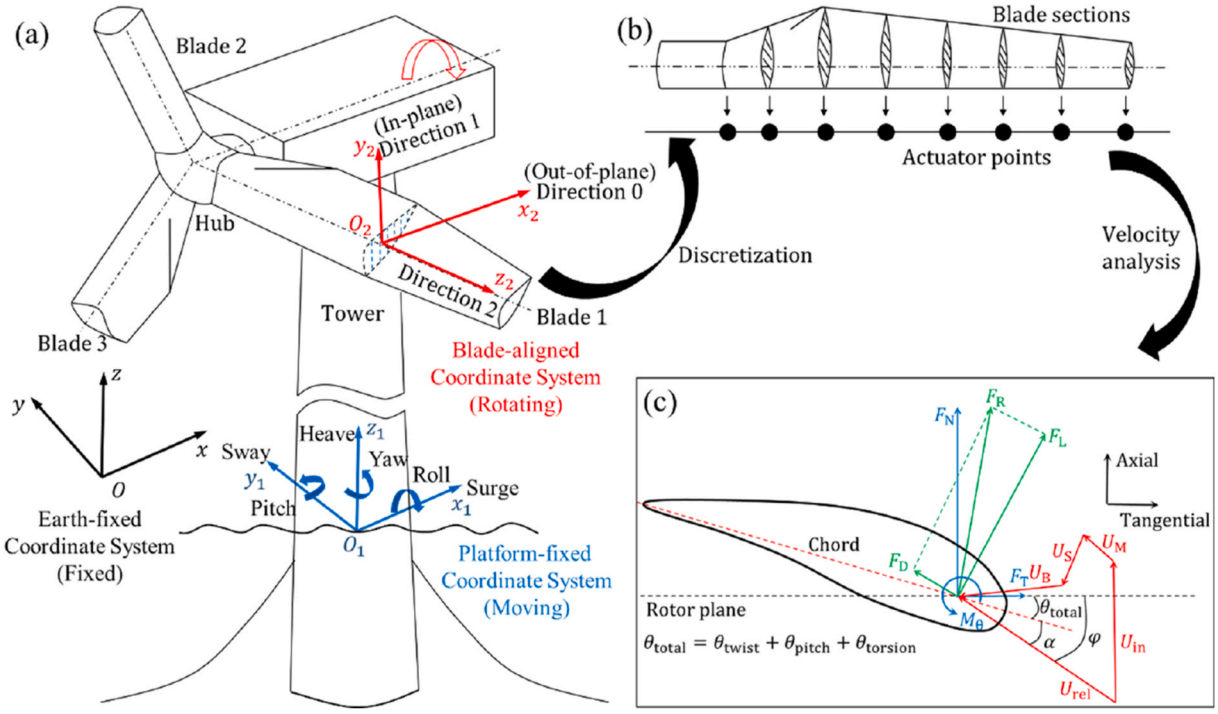

Fig. A.1. Schematic diagram of modified actuator line model for wind turbine blades.

To accurately describe the velocity relationship in the modified ALM, three coordinate systems are defined for the FOWT blades, as shown in Fig. A1(a). The blades are discretized into a series of actuator points, each representing a two-dimensional blade section. The velocity relationship at the actuator point is illustrated in Fig. A1(c). To calculate the aerodynamic loads, the relative wind speed ($\boldsymbol{U}_{\mathrm{rel}}$) and the local angle of attack (α) must be determined first. From Fig. A1(c), $\boldsymbol{U}_{\mathrm{rel}}$ is given by Eqs. (A.1) ~ (A.2).

$$\boldsymbol{U}_{\mathrm{rel}} = \boldsymbol{U}_{\mathrm{in}} + \boldsymbol{U}_{\mathrm{b}} + \boldsymbol{U}_{\mathrm{m}} + \boldsymbol{U}_{\mathrm{s}} \tag{A.1}$$

$$\boldsymbol{U}_{\mathrm{b}} = \boldsymbol{\Omega} \times \boldsymbol{r} \tag{A.2}$$

where $\boldsymbol{U}_{\mathrm{in}}$ represents the inflow wind speed, $\boldsymbol{U}_{\mathrm{b}}$ denotes the rotational speed obtained from the cross product of the rotor's angular speed ($\boldsymbol{\Omega}$) and the

distance vector ($\boldsymbol{r}$) from the rotor hub to the actuator point. $\boldsymbol{\Omega}$ is regulated by the GT controller in response to changes in the inflow wind speed. $\boldsymbol{U}_{\mathrm{m}}$ and $\boldsymbol{U}_{\mathrm{s}}$ represent the additional speeds caused by the platform's 6DoF motions and blade structural deformation, respectively.

Similarly, from Fig. A1(c), α can be determined by Eqs. (A.3) ~ (A.5).

$$\phi = \tan^{-1}(U_a / U_t) \tag{A.3}$$

$$\alpha = \phi - \theta_{\mathrm{t}} \tag{A.4}$$

$$\theta_{\mathrm{t}} = \theta_{\mathrm{p}} + \theta_{\mathrm{w}} + \theta_{\mathrm{s}} \tag{A.5}$$

where ϕ represents the local inflow angle, calculated as the tangent of the ratio of U_a and U_t, the projection components of $\boldsymbol{U}_{\mathrm{rel}}$ along the x-axis and y-axis in the blade-aligned coordinate system. θ_{p} denotes the blade pitch angle, which is regulated by the BP controller. θ_{w} the local twist angle at the blade section, and θ_{s} the local torsional angle induced by blade deformation.

Based on α, the lift coefficient (C_{L}) and drag coefficient (C_{D}) are obtained by interpolating the aerodynamic database for the blade airfoil. The aerodynamic load $\boldsymbol{f}$ acting on the actuator point is then calculated using the equation below:

$$\boldsymbol{f} = (\boldsymbol{L}, \boldsymbol{D}) = \frac{1}{2}\rho_{\mathrm{a}}|U_{\mathrm{rel}}|^2 c\mathrm{d}r(C_{\mathrm{L}}\boldsymbol{e}_{\mathrm{L}} + C_{\mathrm{D}}\boldsymbol{e}_{\mathrm{D}}) \tag{A.6}$$

where $\boldsymbol{L}$ and $\boldsymbol{D}$ represent the aerodynamic lift and drag forces on the airfoil section, ρ_{a} denotes the air density, c represents the chord length, dr indicates the length of the airfoil segment, $\boldsymbol{e}_{\mathrm{L}}$ and $\boldsymbol{e}_{\mathrm{D}}$ signify the unit vectors in the x and y directions in the blade-aligned coordinate system. Tip loss corrections proposed by Shen et al. (2005) are also considered.

Furthermore, by integrating the aerodynamic loads along the blade's radial direction, the aerodynamic thrust (T_{R}) and power (P_{R}) of the wind turbine can be determined.

$$T = \sum_{i=1}^{N_{\mathrm{p}}} \boldsymbol{D}_i \bullet \boldsymbol{x}_0 \tag{A.7}$$

$$P = \sum_{i=1}^{N_{\mathrm{p}}} (\boldsymbol{L}_i \times \boldsymbol{r}_i) \bullet \boldsymbol{\Omega} \tag{A.8}$$

where $\boldsymbol{L}_i$ and $\boldsymbol{D}_i$ represent the lift and drag forces acting on the ith actuator point, N_{p} is the number of actuator points, $\boldsymbol{r}_i$ is the distance vector from the blade root to the ith actuator point, and $\boldsymbol{x}_0$ is the unit vector in the x-direction in the earth-fixed coordinate system.

The modified actuator line model is also employed to consider the nacelle and tower of the FOWTs. As shown in Fig. A2(a), the nacelle is simplified into a cylinder with a hemispherical cap, with the base area of the cylinder matching the projected area of the nacelle on the plane of turbine rotation. The nacelle is divided into cylindrical segments at equal intervals, each replaced by an actuation point. Similarly, the wind turbine tower is discretized into cylinders at equal intervals, each represented by an actuation point, as shown in Fig. A2(b). By calculating the relative wind speed and angle of attack at each actuation point, the corresponding lift and drag coefficients are interpolated to determine the aerodynamic loads. Integration yields the total aerodynamic loads acting on the entire nacelle and tower.

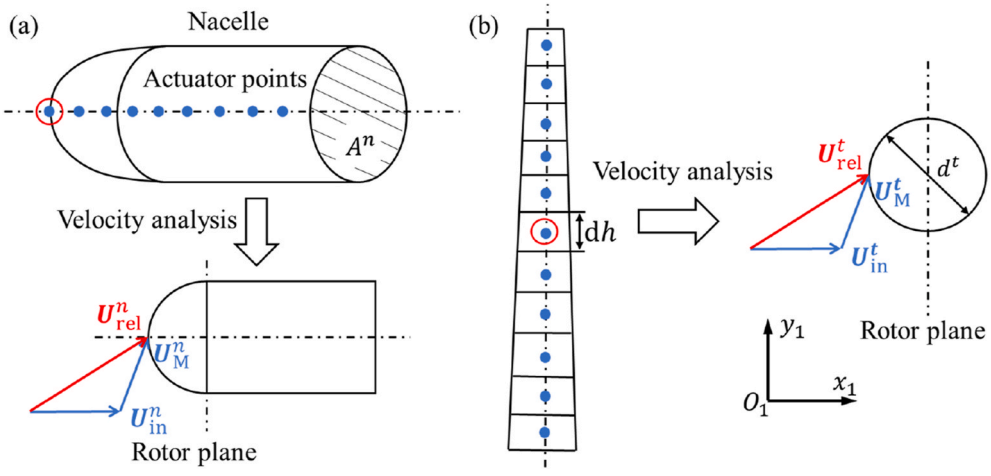

Fig. A.2. Schematic diagram of modified actuator line model for nacelle and tower of the FOWT.

To consider the wind turbine's impact on the flow field, it is essential to project the aerodynamic forces from the blades, nacelle, and tower onto the flow field. This projection uses a regularization kernel function, η_ε, to ensure a smooth transition of the aerodynamic force from a point to a spherical region, mitigating potential numerical errors. The kernel function is defined as:

$$\eta_\varepsilon(d) = \frac{1}{\varepsilon^3 \pi^{3/2}} \exp\left[-\left(\frac{d}{\varepsilon}\right)^2\right] \tag{A.9}$$

The body force at a given point (x, y, z) in the flow field is determined by:

$$f_\varepsilon(x,y,z,t)=\sum_{i=1}^{N_p} f(x_i,y_i,z_i,t)\frac{1}{\varepsilon^3\pi^{3/2}}exp\left[-\left(\frac{d_i}{\varepsilon}\right)^2\right] \tag{A.10}$$

where d_i represents the distance from the given point to the ith actuator point. The constant parameter ε defines the width of the projection region and significantly impacts computational fidelity. In this study, ε is set to 4.0, equivalent to twice the local grid side length, a value recommended for stable numerical solutions (Gao and Wang, 2020).

Appendix B. Structure model

Large wind turbine blades, with their high aspect ratio, primarily exhibit bending deformations and negligible shear deformations. Assuming small deformations and plane sections, the Euler-Bernoulli beam theory is used for structural analysis (Bauchau and Craig, 2009).

In the structure model, the blades are modelled as cantilever beams. A multi-degree-of-freedom model using a discrete reference frame calculates bending deformations in the flap-wise (x_2-axis) and edgewise (y_2-axis) directions, as well as torsional deformations around the blade's axis (z_2-axis). The FEM discretizes the wind turbine blades, dividing the continuous beam structure into a discrete system of elements connected by finite nodes, as shown in Fig. A3. Each beam element has two nodes, each with three degrees of freedom: flap-wise deformation (δ_0), edgewise deformation (δ_1), and torsional deformation (δ_θ). The internal shape of the beam elements is described using Hermite shape functions (Petera and Pittman, 1994):

$$y(x,t)=\varphi_1 y_i+\varphi_2 y_i'+\varphi_3 y_{i+1}+\varphi_4 y_{i+1}' \tag{B.1}$$

where y_i and y_{i+1} are the displacements at two end nodes, y_i' and y_{i+1}' are the rotations at the two end nodes, and φ_1, φ_2, φ_3, and φ_4 represent the Hermite polynomials.

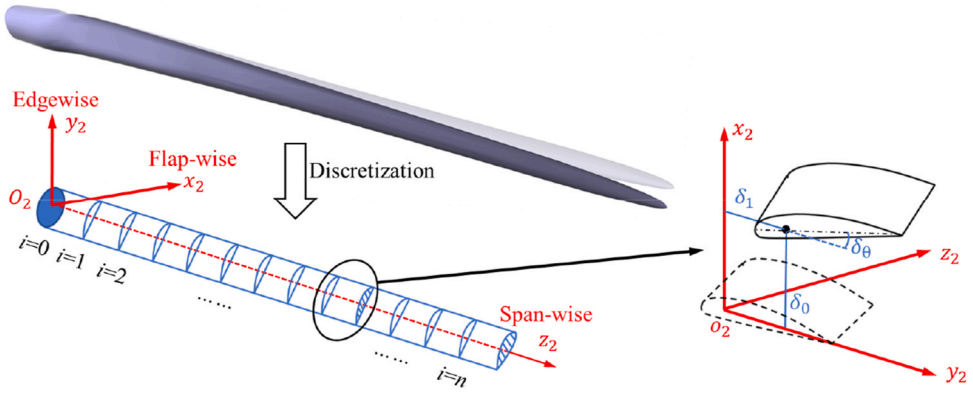

Fig. B.1. Schematic diagram of structural model for wind turbine blades.

For the structural part, the structural dynamics equations based on the principle of virtual work are chosen as the governing equations:

$$[\mathbf{M}]\ddot{\boldsymbol{y}}+[\mathbf{C}]\dot{\boldsymbol{y}}+[\mathbf{K}]\boldsymbol{y}=\boldsymbol{F}(t) \tag{B.2}$$

where $[\mathbf{M}]$, $[\mathbf{C}]$, and $[\mathbf{K}]$ represent the global mass, damping, and stiffness matrices, respectively, $\boldsymbol{F}$ is the time-varying external load vector acting on the blade element, and $\boldsymbol{y}$ denotes the displacements at the element nodes, including linear displacements and rotational angles:

$$\boldsymbol{y}=[\boldsymbol{y_1}\quad \boldsymbol{y_2}\quad \boldsymbol{y_\theta}]^{\mathrm{T}} \tag{B.3}$$

where $\boldsymbol{y_1}$, $\boldsymbol{y_2}$ and $\boldsymbol{y_\theta}$ represent the vectors of displacement along the flap-wise direction, edgewise direction, and angular displacement of the blade element nodes, respectively. Additionally, $[\mathbf{C}]$ is considered a linear combination of $[\mathbf{M}]$ and $[\mathbf{K}]$.

$$[\mathbf{C}]=a_0[\mathbf{M}]+a_1[\mathbf{K}] \tag{B.4}$$

$$\begin{bmatrix}a_0\\a_1\end{bmatrix}=\frac{2\xi}{f_{n1}+f_{n2}}\begin{bmatrix}2\pi f_{n1}f_{n2}\\1/2\pi\end{bmatrix} \tag{B.5}$$

Here, ξ represents the blade damping ratio, while f_{n1} and f_{n2} denote the first and second natural frequencies of the blade, respectively.

Appendix C. Hydrodynamic model

A CFD code, naoe-FOAM-SJTU (Wang et al., 2019), is used to calculate the hydrodynamic responses of the floating platform with a mooring system. This code has been widely applied to various fluid-structure interaction problems in marine engineering, demonstrating high accuracy and reliability (Huang, 2021; Cao and Wan, 2017; Zhuang and Wan, 2019; Wang and Wan, 2019). It includes several modules, including numerical wave tank, 6DoF motion solver, and mooring system module. A brief introduction to the 6DoF and mooring system modules is provided in this appendix.

As illustrated in Fig. C1(a), two coordinate systems are defined for the calculation of platform's 6DoF motions. The 6DoF motions of the platform in the earth-fixed coordinate system (x-y-z) is represented by $\boldsymbol{\eta}=(\boldsymbol{\eta_1},\boldsymbol{\eta_2})=(x_1,x_2,x_3,\phi,\theta,\psi)$, corresponding to the platform's surge, sway, heave, roll,

pitch, and yaw motions, respectively. The motion velocities in different directions under the platform-fixed coordinate system (x_1-y_1-z_1) are denoted by $\boldsymbol{\nu} = (\boldsymbol{\nu_1}, \boldsymbol{\nu_2}) = (u, v, w, p, q, r)$. The displacements, forces, and velocities can be transformed between the earth-fixed and platform-fixed coordinate systems through the following transformation matrices:

$$\mathbf{J_1} = \begin{bmatrix} \cos\theta\cos\psi & \sin\phi\sin\theta\cos\psi & \cos\phi\sin\theta\cos\psi + \sin\phi\cos\psi \\ \cos\theta\sin\psi & \sin\phi\sin\theta\sin\psi & \cos\phi\sin\theta\sin\psi - \sin\phi\cos\psi \\ -\sin\theta & \sin\phi\cos\theta & \cos\phi\cos\theta \end{bmatrix} \tag{C.1}$$

$$\mathbf{J_2} = \begin{bmatrix} 1 & \sin\phi\tan\theta & \cos\phi\tan\theta \\ 0 & \cos\phi & -\sin\theta \\ 0 & \sin\phi/\cos\theta & \cos\phi/\cos\theta \end{bmatrix} \tag{C.2}$$

$$\boldsymbol{\nu} = (\boldsymbol{\nu}_1, \boldsymbol{\nu}_2) = \left(\mathbf{J}_1^{-1} \bullet \dot{\boldsymbol{\eta}}_1, \mathbf{J}_2^{-1} \bullet \dot{\boldsymbol{\eta}}_2\right) \tag{C.3}$$

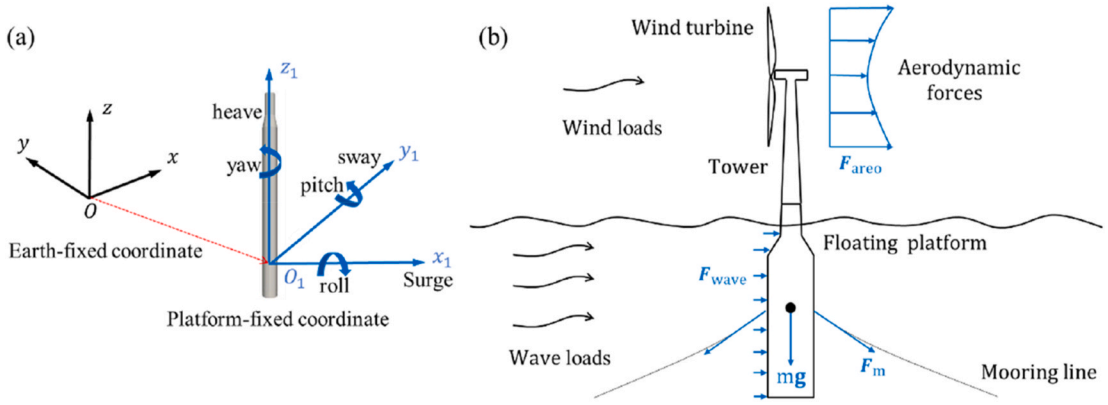

Fig. C.1. Schematic diagram of hydrodynamic model: (a) Coordinate systems; (b) External forces acting on the floating platform.

Figure C1(b) illustrates the external loads on a floating support platform, including gravity ($m\boldsymbol{g}$), aerodynamic force ($\boldsymbol{F}_a$), wave force ($\boldsymbol{F}_w$), and mooring tension ($\boldsymbol{F}_m$). By solving the rigid body motion equations in the platform-fixed coordinate system, $\boldsymbol{\nu}$ is obtained. Integrating $\boldsymbol{\nu}$ over time determines the platform's displacement. Using the transformation matrix, $\boldsymbol{\eta}$ can be obtained.

Additionally, the platform's 6DoF motion is implemented using a dynamic mesh technique. When the platform moves, the mesh topology in the computational domain remains unchanged, but the distances between mesh nodes change. The positions of the mesh nodes are determined by solving a Laplace equation with variable diffusivity γ:

$$\nabla \bullet (\gamma \nabla \boldsymbol{X}_g) = 0, \gamma = \frac{1}{r^2} \tag{C.4}$$

where $\boldsymbol{X}_g$ represents the displacements of mesh nodes, r is the distance between the cell centre and the platform.

The piecewise extrapolation method (PEM) is used to solve the mooring system. As shown in Figure C2(a), the mooring line is divided into segments. By conducting a static analysis on each segment and applying boundary conditions, the tension and shape of each segment are sequentially extrapolated and calculated. Fig. C2(b) illustrates the forces acting on a mooring segment, allowing for the establishment of a static equilibrium equation.

$$\begin{cases} T_{x,i+1} - T_{x,i} - F_i \mathrm{d}s \bullet \cos\varphi_{i+1} - D_i \mathrm{d}s \bullet \sin\varphi_{i+1} = \rho g A \Delta z' \bullet \cos\varphi_{i+1} \\ T_{z,i+1} - T_{z,i} - F_i \mathrm{d}s \bullet \sin\varphi_{i+1} + D_i \mathrm{d}s \bullet \cos\varphi_{i+1} - w_i \mathrm{d}l = \rho g A \Delta z' \bullet \sin\varphi_{i+1} \end{cases} \tag{C.5}$$

where T represents the mooring tension, φ is the angle between the mooring tension and its horizontal component, and F and D denote the tangential and normal forces on the mooring segment due to fluid forces, respectively, which can be calculated using the Morison equation. dl and ds represent the length of the anchor chain unit before and after stretching, respectively, w is the wet weight of the mooring segment in water, ρ is the fluid density, g is the acceleration due to gravity, A is the cross-sectional area of the mooring segment, and $\Delta z'$ is the vertical distance between two nodes of the mooring segment.

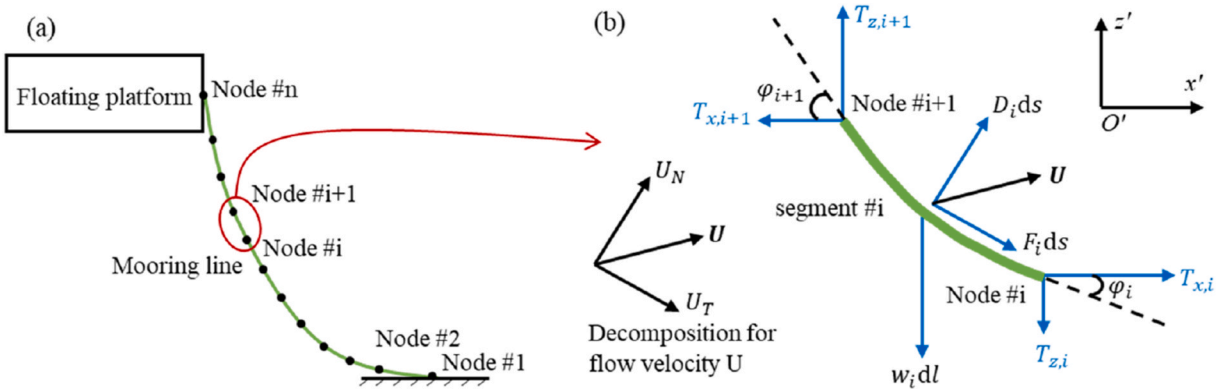

Fig. C.2. (a) Mooring segment; (b) Forces acting on a mooring segment.

References

Bauchau, O.A., Craig, J.I., 2009. Euler-Bernoulli beam theory. In: Structural Analysis. Springer Netherlands, Dordrecht, pp. 173–221.

Bošnjaković, M., Katinić, M., Santa, R., Marić, D., 2022. Wind turbine technology trends. Appl. Sci. 12 (17), 8653.

Cao, H., Wan, D., 2017. Benchmark computations of wave run-up on single cylinder and four cylinders by naoe-FOAM-SJTU solver. Appl. Ocean Res. 65, 327–337.

Cheng, P., Huang, Y., Wan, D., 2019. A numerical model for fully coupled aero-hydrodynamic analysis of floating offshore wind turbine. Ocean Engineering 173, 183–196.

Cordle, A., Jonkman, J., 2011. State of the art in floating wind turbine design tools. In: ISOPE International Ocean and Polar Engineering Conference. ISOPE pp. ISOPE-I.

Díaz, H., Soares, C.G., 2020. Review of the current status, technology and future trends of offshore wind farms. Ocean Engineering 209, 107381.

DNV. Bladed n.d. https://www.dnv.com/services/wind-turbine-design-software-bladed-3775 (accessed April 8, 2024).

DTU. HAWC2. n.d. www.hawc2.dk. (Accessed 8 April 2024).

Gao, Z.T., Wang, T.G., 2020. Experimental validation and improvement of actuator line model in the large-eddy simulation of wind-turbine wakes. In: IOP Conference Series: Earth and Environmental Science, vol. 463. IOP Publishing, 012113, 1.

Ha, K., Truong, H.V.A., Dang, T.D., Ahn, K.K., 2021. Recent control technologies for floating offshore wind energy system: a review. International Journal of Precision Engineering and Manufacturing-Green Technology 8, 281–301.

Hegseth, J.M., Bachynski, E.E., 2019. A semi-analytical frequency domain model for efficient design evaluation of spar floating wind turbines. Mar. Struct. 64, 186–210.

Huang, Y., 2021. Numerical Investigation on Coupled Aero-Hydro-Elastic Responses and Wake Interference of Floating Wind Turbines. PhD thesis. Shanghai Jiao Tong University, China.

Huang, Y., Wan, D., 2019. Investigation of interference effects between wind turbine and spar-type floating platform under combined wind-wave excitation. Sustainability 12 (1), 246.

Huang, Y., Wan, D., 2020. Numerical analysis of aeroelastic responses of wind turbine under uniform inflow. In: International Conference on Offshore Mechanics and Arctic Engineering, vol. 84416. American Society of Mechanical Engineers. V009T09A041.

Huang, Y., Wan, D., Hu, C., 2021. Numerical analysis of aero-hydrodynamic responses of floating offshore wind turbine considering blade deformation. In: ISOPE International Ocean and Polar Engineering Conference. ISOPE. ISOPE-I.

Huang, Y., Xiao, Q., Wan, D., 2022. Wake interaction between two floating offshore wind turbines with blade deformation. In: International Conference on Offshore Mechanics and Arctic Engineering, vol. 85932. American Society of Mechanical Engineers. V008T09A014.

Huang, Y., Zhao, W., Wan, D., 2023. Wake interaction between two spar-type floating offshore wind turbines under different layouts. Phys. Fluids 35 (9).

Jasak, H., 2009. OpenFOAM: open source CFD in research and industry. Int. J. Nav. Archit. Ocean Eng. 1 (2), 89–94.

Jonkman, J., 2010. Definition of the Floating System for Phase IV of OC3 (No. NREL/TP-500-47535). National Renewable Energy Lab. (NREL), Golden, CO (United States).

Jonkman, J., Butterfield, S., Musial, W., Scott, G., 2009. Definition of a 5-MW Reference Wind Turbine for Offshore System Development. National Renewable Energy Lab. (NREL), Golden, CO (United States) (No. NREL/TP-500-38060).

Karimi, M., Hall, M., Buckham, B., Crawford, C., 2017. A multi-objective design optimization approach for floating offshore wind turbine support structures. Journal of Ocean Engineering and Marine Energy 3, 69–87.

Li, P., Cheng, P., Wan, D.C., Xiao, Q., 2015. Numerical simulations of wake flows of floating offshore wind turbines by unsteady actuator line model. In: Proceedings of the 9th International Workshop on Ship and Marine Hydrodynamics, pp. 26–28. Glasgow, UK.

Liu, Y., Xiao, Q., Incecik, A., Peyrard, C., Wan, D., 2017. Establishing a fully coupled CFD analysis tool for floating offshore wind turbines. Renew. Energy 112, 280–301.

López-Queija, J., Robles, E., Jugo, J., Alonso-Quesada, S., 2022. Review of control technologies for floating offshore wind turbines. Renew. Sustain. Energy Rev. 167, 112787.

Manwell, J.F., McGowan, J.G., Rogers, A.L., 2010. Wind Energy Explained: Theory, Design and Application. John Wiley & Sons.

MARINTEK. Sima. www.windbench.net/models-offshore/sima, 2016–. (Accessed 8 April 2024).

MBDyn. https://www.mbdyn.org/, 2024–. (Accessed 8 April 2024).

Ning, X., Wan, D., 2019. LES study of wake meandering in different atmospheric stabilities and its effects on wind turbine aerodynamics. Sustainability 11 (24), 6939.

NREL. Fast. n.d. https://www.nrel.gov/wind/nwtc/fast.html. (Accessed 8 April 2024).

Obhrai, C., Kalvig, S., Gudmestad, O.T., 2012. A review of current guidelines and research on wind modelling for the design of offshore wind turbines. In: ISOPE International Ocean and Polar Engineering Conference. ISOPE pp. ISOPE-I.

Orcina. Orcaflex n.d. https://www.orcina.com/webhelp/OrcaFlex/Default.htm (accessed April 8, 2024).

Otter, A., Murphy, J., Pakrashi, V., Robertson, A., Desmond, C., 2022. A review of modelling techniques for floating offshore wind turbines. Wind Energy 25 (5), 831–857.

Paterson, E.G., Wilson, R.V., Stern, F., 2003. General-purpose Parallel Unsteady RANS Ship Hydrodynamics Code: CFDSHIP-IOWA. IIHR Report, p. 432.

Pegalajar-Jurado, A., Borg, M., Bredmose, H., 2018. An efficient frequency-domain model for quick load analysis of floating offshore wind turbines. Wind Energy Science 3 (2), 693–712.

Petera, J., Pittman, J.F.T., 1994. Isoparametric hermite elements. Int. J. Numer. Methods Eng. 37 (20), 3489–3519.

Quallen, S., Xing, T., 2016. CFD simulation of a floating offshore wind turbine system using a variable-speed generator-torque controller. Renew. Energy 97, 230–242.

Robertson, A., Jonkman, J., Vorpahl, F., Popko, W., Qvist, J., Frøyd, L., et al., 2014. Offshore code comparison collaboration continuation within IEA wind task 30: phase II results regarding a floating semisubmersible wind system. In: International Conference on Offshore Mechanics and Arctic Engineering, vol. 45547. American Society of Mechanical Engineers. V09BT09A012.

Robertson, A.N., Wendt, F., Jonkman, J.M., Popko, W., Dagher, H., Gueydon, S., et al., 2017. OC5 project phase II: validation of global loads of the DeepCwind floating semisubmersible wind turbine. Energy Proc. 137, 38–57.

Robertson, A.N., Gueydon, S., Bachynski, E., Wang, L., Jonkman, J., Alarcon, D., et al., 2020. OC6 Phase I: investigating the underprediction of low-frequency hydrodynamic loads and responses of a floating wind turbine. J. Phys. Conf. 1618 (3), 032033. IOP Publishing.

Sabalcore. StarCCM. https://www.sabalcore.com/vertical-markets/engineering/star-ccm/, 2024–. (Accessed 8 April 2024).

Sarpkaya, T., 1981. Morison's Equation and the Wave Forces on Offshore Structures, p. 270. Carmel, CA, USA: Naval Civil Engineering Laboratory.

Sebastian, T., Lackner, M.A., 2012. Development of a free vortex wake method code for offshore floating wind turbines. Renew. Energy 46, 269–275.

Shah, K.A., Meng, F., Li, Y., Nagamune, R., Zhou, Y., Ren, Z., Jiang, Z., 2021. A synthesis of feasible control methods for floating offshore wind turbine system dynamics. Renew. Sustain. Energy Rev. 151, 111525.

Shen, W.Z., Mikkelsen, R., Sørensen, J.N., Bak, C., 2005. Tip loss corrections for wind turbine computations. Wind Energy: An International Journal for Progress and Applications in Wind Power Conversion Technology 8 (4), 457–475.

Smagorinsky, J., 1963. General circulation experiments with the primitive equations: I. The basic experiment. Mon. Weather Rev. 91 (3), 99–164.

Suzuki, A., Hansen, A., 1999. Generalized dynamic wake model for YawDyn. In: 37th Aerospace Sciences Meeting and Exhibit, p. 41.

Tran, T.T., Kim, D.H., 2015a. The aerodynamic interference effects of a floating offshore wind turbine experiencing platform pitching and yawing motions. J. Mech. Sci. Technol. 29, 549–561.

Tran, T.T., Kim, D.H., 2015b. The coupled dynamic response computation for a semi-submersible platform of floating offshore wind turbine. J. Wind Eng. Ind. Aerod. 147, 104–119.
Tran, T.T., Kim, D.H., 2016. A CFD study into the influence of unsteady aerodynamic interference on wind turbine surge motion. Renew. Energy 90, 204–228.
Tran, T.T., Kim, D.H., 2018. A CFD study of coupled aerodynamic-hydrodynamic loads on a semisubmersible floating offshore wind turbine. Wind Energy 21 (1), 70–85.
Troldborg, N., 2009. Actuator Line Modeling of Wind Turbine Wakes.
Truong, H.V.A., Dang, T.D., Vo, C.P., Ahn, K.K., 2022. Active control strategies for system enhancement and load mitigation of floating offshore wind turbines: a review. Renew. Sustain. Energy Rev. 170, 112958.
Wang, J., Wan, D., 2019. Naoe-foam-sjtu solver for ship flows and ocean engineering flows. In: MARINE VIII: Proceedings of the VIII International Conference on Computational Methods in Marine Engineering. CIMNE, pp. 23–34.
Wang, J.H., Zhao, W.W., Wan, D.C., 2019. Development of naoe-FOAM-SJTU solver based on OpenFOAM for marine hydrodynamics. J. Hydrodyn. 31, 1–20.
Wood Group. Flexcom. n.d. https://www.woodplc.com/capabilities/digital-and-technology/software,-applications-and-analytics/flexcom. (Accessed 8 April 2024).
Yang, L., Liao, K., Ma, Q., Ma, G., Sun, H., 2023. Investigation of wake characteristics of floating offshore wind turbine with control strategy using actuator curve embedding method. Renew. Energy 218, 119255.
Zhang, Y., Kim, B., 2018. A fully coupled computational fluid dynamics method for analysis of semi-submersible floating offshore wind turbines under wind-wave excitation conditions based on OC5 data. Applied sciences 8 (11), 2314.
Zhuang, Y., Wan, D., 2019. Numerical simulation of ship motion fully coupled with sloshing tanks by naoe-FOAM-SJTU solver. Eng. Comput. 36 (8), 2787–2810.